**Universidade de Aveiro** Departamento de Química
**2017**

**JESSE
CORNELIUS
RIEDL**

# EFEITO DE DOPAGEM DE IÕES $Li^+$ EM NANOPARTÍCULAS DE $Y_20_3$:$Yb^{3+}$/$Er^{3+}$ COM CONVERSÃO DE ENERGIA ASCENDENTE

# EFFECT ON THE UP-CONVERSION EMISSION OF $Li^+$ DOPING OF $Y_2O_3$:$Yb^{3+}$/$Er^{3+}$ NANOPARTICLES

Dissertação apresentada à Universidade de Aveiro para cumprimento dos requisitos necessários à obtenção do grau de Mestrado em Química / Functionalized Advanced Materials and Engineering (FAME), realizada sob a orientação científica dos Doutores João Rocha e Luís D. Carlos Professores Catedráticos dos Departamentos de Química e de Física da Universidade de Aveiro

## o júri

| | |
|---|---|
| presidente | Prof. Doutora Ana Margarida Madeira Viegas de Barros Timmons<br>professora auxiliar do Departamento de Química da Universidade de Aveiro |
| | Prof. Doutor Tito Trindade<br>professor associado com Agregação do Departamento de Química da Universidade de Aveiro |
| | Prof. Doutor João Rocha<br>professor Catedrático do Departamento de Química da Universidade de Aveiro |

**agradecimentos**

Quero expressar a minha gratidão ao Prof. João Rocha e ao Prof. Luís António Ferreira Martins Dias Carlos pela supervisão desta tese de Mestrado e por todas as discussões úteis.

Desejo, também, agradecer ao Dr. Mengistie Debasu que me ajudou em todas as questões técnicas e experimentais sobre a preparação de amostras, medições de fotoluminescência e de fluxo radiante usando uma esfera integradora. Pude sempre contar com sua experiência prática e apreciei a agradável atmosfera de trabalho com ele.

Devo, também, grande reconhecimento ao apoio no uso de métodos de caracterização no departamento de Química, dado pela Dra. Maria do Rosário Teixeira Soares (XRD) e Dra. Maria Celeste Coimbra Azevedo (FTIR e TGA), e no,  Departamento de Materiais, dado pela Dra. Marta Ascenção Carmona Ferro (microscopia eletrônica).

Desejo, também, agradecer ao financiamento pelo programa Erasmus Mundus e ao mestrado europeu FAME (Functionalized Advanced Materials and Engineering).

Finalmente, gostaria de agradecer ao Laboratório Central de Análises da Universidade de Aveiro e á sua Directora Prof. Eduarda Pereira, por ter efetuado as análises de ICP-AES, e ao Centro de Tecnologia Mecânica e Automação (TEMA) pelos dados de XPS.

**palavras-chave**

IÕES DE TERRAS RARAS; IÕES LÍTIO; ÓXIDOS; NANOCRISTAIS; RENDIMENTO QUÂNTICO DE EMISSÃO; CONVERSÃO ASCENDENTE DE ENERGIA; CO-PRECIPITAÇÃO; REAÇÃO DE ESTADO SÓLIDO

**resumo**

O aumento da emissão visível sob excitação no infravermelho-próximo (processo de conversão ascendente de energia) em nanopartículas de $Y_2O_3$: $Yb^{3+}/Er^{3+}/Li^{+}$ é investigado e quantificado. Usam-se os métodos de co-precipitação e reação de estado sólido, para lograr a incorporação efetiva de $Li^{+}$ na rede do hospedeiro $Y_2O_3$. Apesar de frequentemente reportado na literatura, o método de co-precipitação não permite incorporar $Li^{+}$ nas nanopartículas, como revelado pela análise elementar. O método de reação de estado sólido permite uma dopagem efetiva das nanopartículas de $Y_2O_3$: $Yb^{3+}/Er^{3+}$ com $Li^{+}$. As medidas de luminescência revelam que o rendimento quântico de emissão (q) das nanopartículas aumenta com o aumento da concentração de $Li^{+}$ até 12,3% molar, sendo os valores q máximos observados para 4,8 e 12,3% molar. Os difractogramas de raios X (XRD) de pós mostram que as amostras são cristalinas, não contendo fases secundárias. O refinamento de Rietveld dos dados de XRD de pós não evidencia a incorporação de iões de $Li^{+}$ na rede hospedeira. No entanto, a espectrometria de emissão atómica por plasma acoplado indutivamente (ICP-AES) e a espectroscopia de fotoeletrões excitados por raios-X (XPS) confirmam que as nanopartículas preparadas por via de reação de estado sólido contêm lítio. Por outro lado, a análise termogravimétrica não mostra uma alteração de massa significativa até 800 °C, o que contraria o argumento frequentemente utilizado segundo o qual o aumento da conversão ascendente de energia se deve à diminuição do número de grupos OH presentes na amostra. O tamanho e a forma das nanopartículas são avaliados por microscopia eletrónica de transmissão e estão de acordo com o tamanho de cristalites obtido por XRD usando a equação de Scherrer, sugerindo que as nanopartículas são monocristais. Verifica-se, ainda, que o tamanho das partículas aumenta com o aumento a concentração de $Li^{+}$. Além do aumento dos rendimentos quânticos por dopagem com iões $Li^{+}$, a relação de intensidades de emissão vermelho/verde pode ser ajustada. Estes materiais podem ser promissores para bio-aplicações e para sensores de temperatura.

**keywords**

RARE-EARTH IONS; LITHIUM IONS; OXIDES; NANOCRYSTALS; EMISSION QUANTUM YIELD; UP-CONVERSION; CO-PRECIPTATION; SOLID STATE REACTION

**abstract**

Near infrared-to-visible up-conversion emission enhancement in $Y_2O_3$: $Yb^{3+}/Er^{3+}/Li^+$ nanoparticles is investigated and quantified. Co-precipitation and solid-state reaction routes are investigated to achieve an effective incorporation of $Li^+$ in the $Y_2O_3$ host lattice. Despite numerous reports in the literature, the co-precipitation method does not allow the $Li^+$ incorporation in the nanoparticles, as revealed by elemental analysis. Solid-state reaction route is shown to be suitable for an effective $Li^+$ doping of $Y_2O_3$: $Yb^{3+}/Er^{3+}$ nanoparticles. Luminescence measurements reveal that the emission quantum yield (q) of the nanoparticles increases with increasing $Li^+$ content up to 12.3 mol%, with the highest q values observed for 4.8 and 12.3 mol%. Powder X-ray diffraction (XRD) patterns show that the samples are crystalline and do not contain secondary phases. Rietveld refinement of powder XRD data does not evidence the incorporation of $Li^+$ in the host lattice. However, inductively coupled plasma atomic emission spectroscopy (ICP-AES) and X-ray photoelectron spectroscopy (XPS) confirm that the nanoparticles prepared by the solid-state reaction route contain lithium. In addition, thermogravimetric analysis shows no significant weight change up to 800 °C, which does not support the often used argument that the up-conversion photoluminescence enhancement is due to the decrease in the number of OH-groups present in the sample. The size and shape of the nanoparticles are assessed by transmission electron microscopy and are in accord with the crystallite size obtained from XRD using Scherrer's equation, suggesting that the nanoparticles are single crystals. Moreover, the particle size increases with increasing $Li^+$ concentration. In addition to the enhancement of quantum yields by $Li^+$ doping, the red/green emission intensity ratio can be controlled. These materials may be promising for bio-application and for temperature sensors.

# CONTENT

# INDEX OF FIGURES

## INDEX OF TABLES

# ABBREVIATIONS

| | |
|---|---|
| 3DOM | Three-dimensional ordered macroporous |
| A.u. | Arbitrary units |
| CTAB | Cetyl trimethylammonium bromide |
| CW | Continuous wave |
| ESA | Excited state absorption |
| ET | Energy transfer |
| FTIR | Fourier transform infrared spectroscopy |
| ICDD | International Centre for Diffraction Data |
| ICP-AES | Inductively coupled plasma atomic emission spectroscopy |
| ICP-OES | Inductively coupled plasma optical emission spectrometry |
| IR | Infrared |
| Ln | Lanthanide |
| MIR | Magnetic resonance imaging |
| NC | Nanocrystal |
| NIR | Near-infrared |
| NP | Nanoparticle |
| PL | Photoluminescence |
| Ppb | Parts per billion |
| SAED | Selected area electron diffraction |
| SEM | Scanning electron microscopy |
| (S)TEM | (Scanning) Transmission electron microscopy |
| TGA | Thermogravimetric analysis |
| UC | Up-conversion |
| UHV | Ultra-high vacuum |
| UV | Ultraviolet |
| XPS | X-ray photoelectron spectroscopy |
| XRD | X-ray diffraction |

# 1 Introduction

Trivalent lanthanide ($Ln^{3+}$) ions exhibit long lifetime of excited states, high quantum yield (>50%) and sharp multi-peak line emissions and higher photostability than conventional luminescent probes, such as quantum dots and fluorescence dyes.

In the past few years photon up-conversion (UC), which is the conversion of low energy photons such as infrared light into visible light, has been extensively studied for $Ln^{3+}$ ions.[1, 2] Applications are for example in the field of temperature sensors [3-7], photovoltaic technologies[8], and bimodal, photoluminescence-magnetic resonance, imaging [9].

Photon up-conversion based on inorganic nanoparticles has been mainly hindered by experimental challenges associated with low up-conversion efficiencies.[10] Figure 1 shows different ways to increase UC efficiency. These are host lattice manipulation, energy transfer modulation, surface Plasmon coupling, photonic crystal engineering, broadband sensitization, and surface passivation. In this project the effect of $Li^{+}$ ion doping is analysed which is attributed to lattice manipulation and energy transfer modulation.

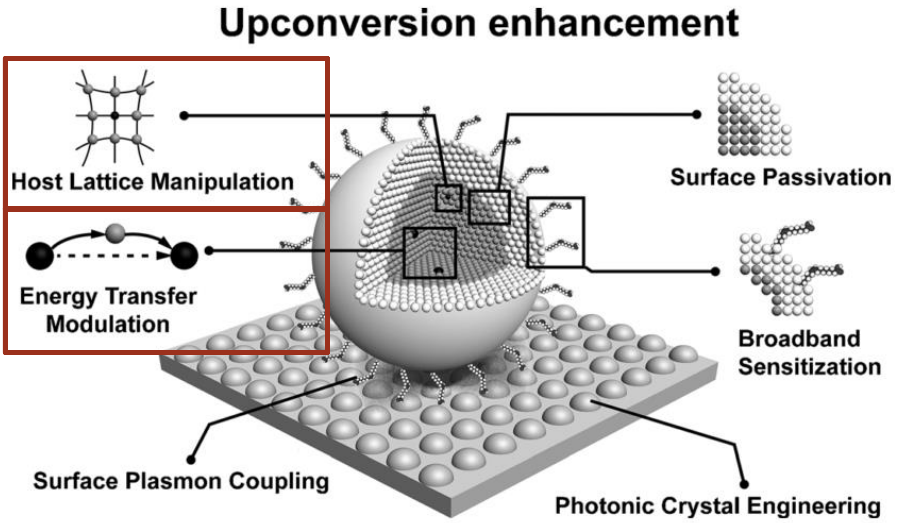

Figure 1: Scheme of main ways to enhance luminescence for Ln-based nanoparticles. [10]

It has been reported that the UC emission intensity of $Ln^{3+}$ ions can be enhanced by doping nanocrystals with $Li^{+}$ ions. [11-69] This effect depends on the host matrices and the activator and sensitizer ions used. The activator ions $Pr^{3+}$, $Nd^{3+}$, $Eu^{3+}$, $Tb^{3+}$, $Ho^{3+}$, $Er^{3+}$, $Tm^{3+}$ and $Yb^{3+}$ can perform an up-conversion process. [70] The effect of $Li^{+}$ on the up-conversion was studied for $Er^{3+}$, $Ho^{3+}$ and $Tm^{3+}$ which possess the mechanism of NIR to visible up-conversion by the excitation of 980 nm (Figure 2). The most often studied activator is $Er^{3+}$ which emits green ($^{2}H_{11/2}$ / $^{4}S_{3/2} \rightarrow {}^{4}I_{15/2}$; 525 nm and 542 nm, respectively) and red ($^{4}F_{9/2} \rightarrow {}^{4}I_{15/2}$;

655 nm) light in the up-conversion process. $Ho^{3+}$ also emits in the red ($^5F_5 \rightarrow {}^5I_8$; 644 nm) and green ($^5S_2$ / $^5F_4 \rightarrow {}^5I_8$; 540 nm) region but at different wavelengths. $Tm^{3+}$ emits in the NIR ($^3H_4 \rightarrow {}^3H_6$; 811 nm), red ($^1G_4 \rightarrow {}^3F_4$; 656 nm) and blue ($^1G_4 \rightarrow {}^3H_6$; 656 nm) region. [52] To enhance the UC emission under excitation with 980 nm, $Yb^{3+}$ is used as sensitizer to further enhance the UC emission efficiency. $Pr^{3+}$ can be used for 488 nm excitation and emits in the UV region (4f5d $\rightarrow {}^3H_4$; 260-360 nm). [53]

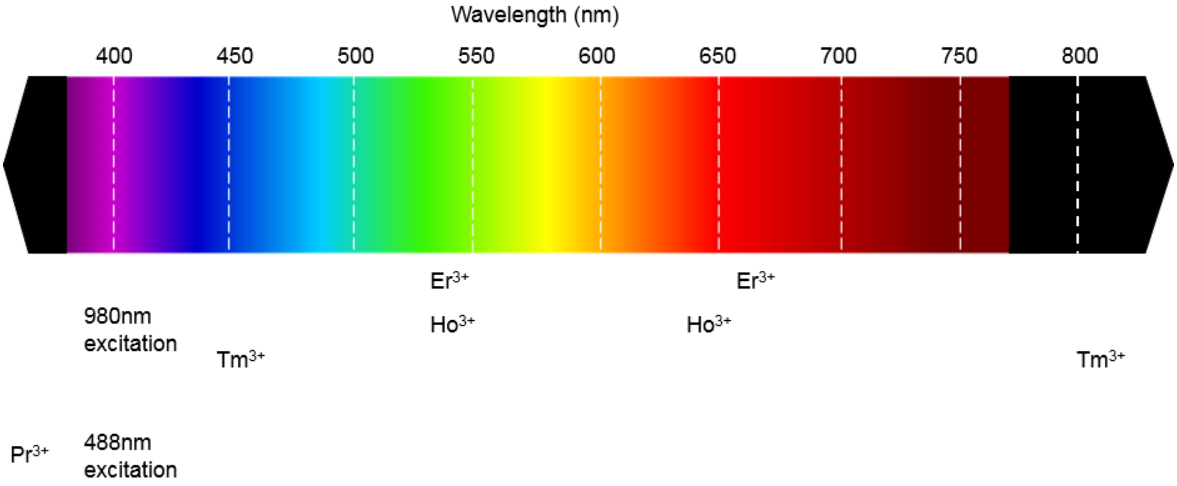

Figure 2: Up-conversion emission of activator ions.

The effect of $Li^+$ doping on up-conversion emission is studied in a series of papers. Table 1 lists the proposed mechanisms of up-conversion enhancement together with the amounts of $Li^+$ doping, activator and sensitizer concentrations in several hosts (Fluorides, oxides, $MO_4$ and glasses). First, properties of different hosts are presented and in particular two example papers which are in connection with the thesis will be analysed more in detail.

Fluorides are among the most studied host matrices for UC, especially $NaYF_4$ [71] and $NaGdF_4$ [72]. As $Na^+$ and trivalent lanthanide ions possess similar ionic radii depending on the coordination number [73], a substitution on the crystal lattice sites is possible. Fluoride host matrices exhibit higher chemical stability than other halides [72] and possess low phonon energies, which is crucial for efficient UC emission. Their crystal structure, which is effected by the doping of $Li^+$ ions, influences the UC properties.

Perovskites and semiconductors belong, among others, to the group of oxide matrices. Perovskite $ABO_3$ oxides possess good piezoelectric, ferroelectric and magnetic properties and are therefore interesting for many applications, [74] including luminescence, as they have high dielectric constant, high charge storage capacity, good insulating property, good chemical and physical stability and relatively low phonon energy (~700 $cm^{-1}$). [70] Metal oxide semiconductor nanomaterials were studied intensively in the past due to their potential applications in solar cells, photocatalysis, and other optoelectronic devices. [75] By combining lanthanides with semiconductors, the optical and other properties can be further improved. $TiO_2$, ZnO and $ZrO_2$ semiconductors are used as hosts for lanthanide doping due to their low phonon energy, large band gap, environmentally friendliness and excellent physical and chemical stability.[70] Their most common use is in electroluminescent devices. However, due to mismatch between the ionic radius of trivalent lanthanide ions and $Ti^{4+}$, $Zn^{2+}$, and $Zr^{4+}$ metal ions, it is difficult to accommodate lanthanide ions in semiconductor matrices. Therefore, lanthanide doping creates charge imbalance and vacancies, which affect the luminescence yield. $Li^+$ ions are used to modify semiconductor host matrices and compensate charge imbalance to improve up-conversion emission $Y_2O_3$ and $Gd_2O_3$ are intensively studied host matrices for luminescence studies as they are biocompatible; have a high mechanical and chemical durability, high thermal stability, excellent optical properties and relatively low phonon cut-off energy (400–500 $cm^{-1}$) [76-79] Moreover, the preparation of phase pure samples is possible by several synthesis methods like conventional solid state reaction at lower temperatures, solution combustion technique, sol–gel technique, hydrothermal technique, etc. [76-80] By controlling the synthesis parameters, the particle size, surface morphology and shape can be controlled. As the ionic radii of trivalent lanthanide ions are similar to $Y^{3+}$ and $Gd^{3+}$ they can be easily incorporated in the lattice. [73] $Gd_2O_3$ is interesting in bio-imaging as a magnetic resonance imaging (MRI) contrast reagent because it possesses paramagnetic behaviour. [79, 80] Different research groups propose different mechanisms for UC enhancement by doping of $Li^+$ ions. [26-31, 40-52, 81, 82] Two example papers that are in connection with this thesis are analysed in detail.

The most common preparation method for $Gd_2O_3$ nanoparticles is solution based (co-precipitation) which includes washing and centrifugation steps. Li *et al.,* [28] prepared $Gd_2O_3$: Yb/Er/Li (10/2/x mol%, x = 0, 2, 4, 6, 8, 10) nanocrystals (NCs) by heating a aqueous solution of deionized water, urea and nitrates of Yb, Gd, Er and Li at 85 °C for 4 hours followed by a separation by centrifugation, washing several times with deionized water and drying at 80 °C. Subsequently, the sample is annealed at 1100 °C for 4 hours. Spherical, monodisperse particles with a mean diameter of 202 nm are obtained and this remain the same after $Li^+$ ions doping, shown in Figure 3 for a1) $Gd_2O_3$: Yb/Er (10/2 mol%) NCs and in a2) for additional 10 mol% Li doping. As shown in Figure 3b) all diffraction peaks of Yb/Er/Li (10/2/x mol%, x = 0, 2, 4, 6, 8, 10) NCs can be well indexed to $Gd_2O_3$ (JCPDS No. 43-1014) and no other impurity peaks can be observed whereas they conclude that doping $Li^+$ ions doesn't change the crystal phase of $Gd_2O_3$ samples. However, they found that the positions of the diffraction peaks shift slightly with increasing doping of $Li^+$ ion concentrations up to 6 mol% and shift towards smaller angles for 8 mol% and to bigger angles again for 10 mol%. However, they didn't use a reference to calibrate the angles wherefore slight changes could result from the error in the measurement. Increased diffraction angles imply smaller lattice constants and vice versa. From this, they conclude that for small amounts of $Li^+$ ions doping into $Gd_2O_3$ NCs, $Li^+$ ions mainly occupy $Gd^{3+}$ crystal lattice sites and for higher doping concentrations, $Li^+$ ions begin to take interstitial sites. They explain this by the smaller radius of $Li^+$ ions (0.09 nm for six coordination) than the radius of $Gd^{3+}$ ions (0.1028 nm), which shrinks the host lattice by substituting the $Gd^{3+}$ ion lattice site and expands the host lattice with occupation of interstitial sites. The optimum $Li^+$ doping concentration is proposed for 4 mol% with a 2 times enhancement of UC emission, taken from the UC luminescence spectra in Figure 3c) and the ratios of UC luminescence enhancement by doping different $Li^+$ ion concentration in Figure 3d). The enhancement is explained by a shrunk unit cell of $Gd_2O_3$ NCs, generated oxygen vacancies, an environment change around the rare earth ion and a decrease of the crystal symmetry around $Er^{3+}$ ions.

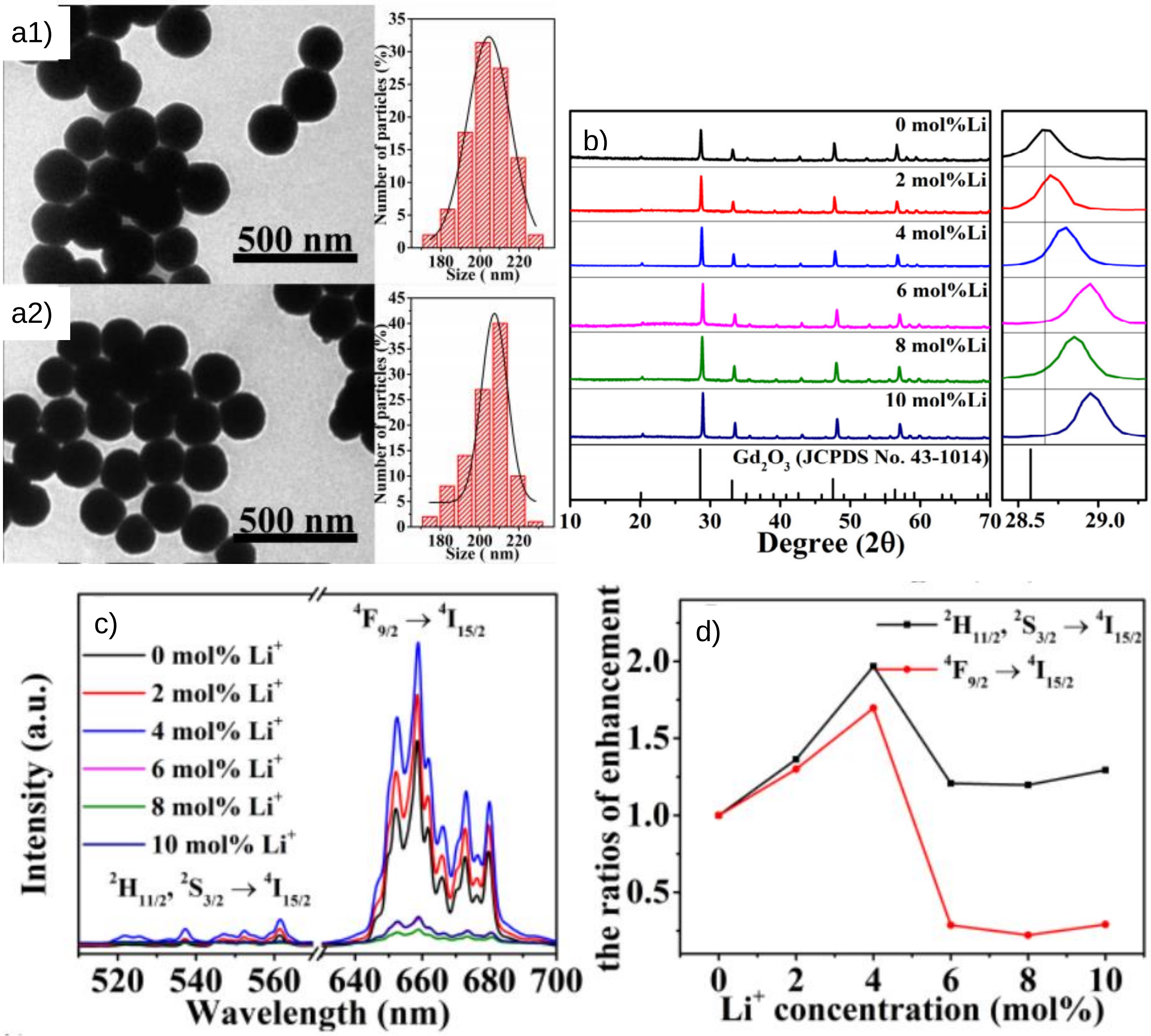

Figure 3: TEM images of a1) $Gd_2O_3$: Yb/Er (10/2 mol%) NCs; a2) $Gd_2O_3$: Yb/Er/Li (10/2/10 mol%); b) XRD patterns and main diffraction peaks of $Gd_2O_3$: Yb/Er/Li (10/2/x mol%, x = 0, 2, 4, 6, 8, 10) NCs; c) UC luminescence spectra of $Gd_2O_3$: Yb/Er/Li (10/2/x mol%, x = 0, 2, 4, 6, 8, 10) NCs excited by 30 $W/cm^2$ 980 nm laser; d) The ratios of UC luminescence enhancement by doping different $Li^+$ ion concentration in $Gd_2O_3$: Yb/Er (10/2 mol%) NCs. All taken from ref. [28]

Only Jia *et al.,* [30] use another synthesis method for the preparation of $Gd_2O_3$ based on a sol-gel route without any washing steps. Nitrate hydrates of Gd, Yb and Ho were mixed in deionized water with $LiCO_3$ at 80 °C. Citric acid (monohydrate) was added in 3 times the amount of the ions and the pH is adjusted to 7 by the addition of ammonium hydroxide. After drying the samples in air at 120 °C for 12 hours, they were calcined in air at 900 °C for 2 hours. Figure 4 depicts TEM images of $Gd_2O_3$: $Yb^{3+}/Ho^{3+}$ nanocrystals in a1) Li-undoped and a2) with 4 mol% $Li^+$ doping concentration. In contrast to a solution based synthesis method the NCs are more agglomerated and less spherical. In Figure 4b) Powder X-ray diffraction patterns are shown for $Gd_2O_3$: $Yb^{3+}/Ho^{3+}$ (2/0.5 mol%) NCs doped with 0 (A2), 1 (B2), 2 (C2), 3 (D2) and 4 (E2) mol% $Li^+$. A crystallite size increase with increasing $Li^+$ content is calculated by Scherrer's equation (2). They found sizes of 26.7, 34.4, 39.0, 42.1 and 48.0 nm for $xLi^+$ doping (x = 0, 1, 2, 3, 4 mol%), respectively. Figure 4c) depicts the up-conversion spectra for $Gd_2O_3$: $Yb^{3+}/Ho^{3+}$ (2/0.5 mol%) NCs doped with 0 (A), 1 (B), 2 (C), 3 (D), 4 (E) mol% $Li^+$ under 976 nm excitation. They found a maximum increase of the UC emission of 10 (green) and 4 (red) times for 3 mol% $Li^+$ doping. However, they only analysed the $Li^+$ doping in the range of 0-4 mol% Li content. They state that the mechanism of the enhancement effect is not completely clear. However, they try to explain it by the occupation of small sized $Li^+$ ions in interstitial $Gd_2O_3$ lattice sites near $Ho^{3+}$ ions to maintain local charge balance between $Ho^{3+}$, $Yb^{3+}$ and $Li^+$ in the $Gd_2O_3$ lattice which leads to a slight modification of the structure, resulting in a lowering of the symmetry of the crystal field around $Ho^{3+}$ ions. Figure 4d) depicts the integral intensity of green (■), red (○) and red/green (▲) up-conversion emission intensities as a function of the $Li^+$ concentration. They found a decrease of the red/green emission intensity ratio with increasing $Li^+$ doping concentration. After a big drop between 0 and 1 mol% $Li^+$ doping the intensity decreases slightly when the $Li^+$ concentration is above 2 mol%. They try to explain the decrease in the ratio with increased $Li^+$ concentration by non-radiative multi-phonon relaxation processes from $^5I_6$ to $^5I_7$ in $Ho^{3+}$ which are weakened with increasing $Li^+$ doping concentration.

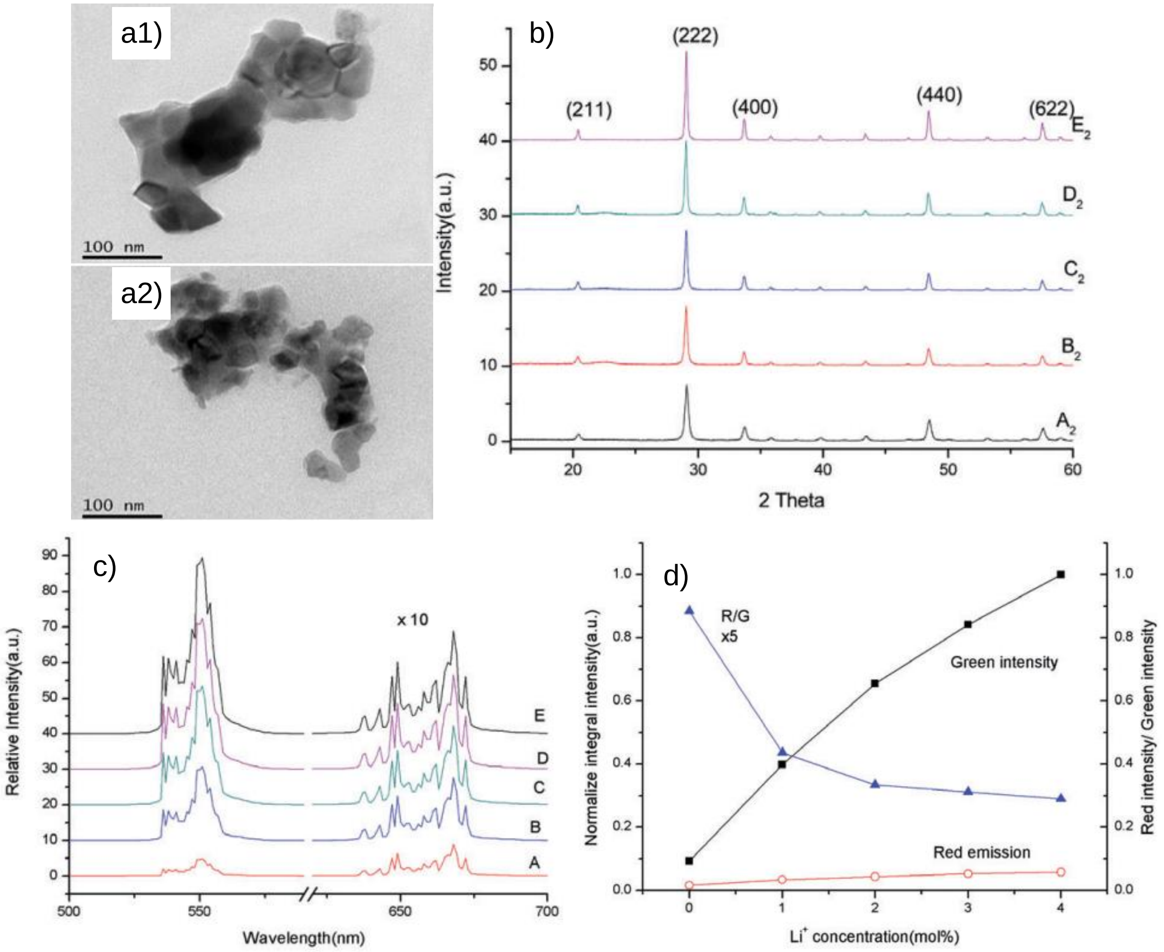

Figure 4: TEM image of $Gd_2O_3$: $Yb^{3+}/Ho^{3+}$ nanocrystals a1) Li-undoped and a2) with 4 mol% $Li^+$ doping concentration; b) Powder X-ray diffraction patterns for $Gd_2O_3$: $Yb^{3+}/Ho^{3+}$ (2/0.5 mol%) NCs doped with 0 (A2), 1 (B2), 2 (C2), 3 (D2) and 4 (E2) mol% $Li^+$; c) up-conversion spectra of for $Gd_2O_3$: $Yb^{3+}/Ho^{3+}$ (2/0.5 mol%) NCs doped with 0 (A), 1 (B), 2 (C), 3 (D), 4 (E) mol% $Li^+$ under 976 nm excitation; d) integral intensity of green (■), red (○) and red/green (▲) up-conversion emission as a function of the $Li^+$ concentration. Taken from ref. [30]

Table 1: Review of effect of Li –doping on up-conversion nanoparticles.

| **Host** | **Sensitizer mol%** | **Activator mol%** | **Li$^+$ doping mol%** | **UC enhancement** | **Synthesis method** | **Remarks** |
|---|---|---|---|---|---|---|
| **Fluorides** | | | | | | |
| **$NaYF_4$** | 20 Yb | 2 Er | 15-85 Li | Decreased | Hydrothermal | Phonon energy of Er$^{3+}$ ions intensified, increased mean distance between ions decrease the energy transfer efficiency between Yb$^{3+}$ and Er$^{3+}$ and increase non-radiation due to shape change [14] |
| **$NaYF_4$** | 2 Yb | 2 Er | 100 Li instead of Na | Blue shift, small decrease | Hydrothermal | Symmetry of the electronic cloud surrounding the RE$^{3+}$ is higher in $LiYbF_4$, weakened polarization effect [15] |
| **$NaYF_4$** | 5 Yb | 1 Er | 30 Li | 7 (green) and 5 (red) | Hydrothermal | Altering of local symmetry, lower intensity of the -OH peak (FTIR) -> small agglomeration of the particles, reduction in non-radiative relaxation rate [16] |
| **$NaYF_4$** | 18 Yb | 2 Er | 4 Li | 2 (green) 3.3 (red) | Hydrothermal | Prolonged lifetime, separation of the Er$^{3+}$ clusters, enlargement of the distance between Er$^{3+}$ and the neighbouring ions [17] |
| **$NaYF_4$** | 18 Yb | 2 Er (+?Tm) | 20-80 Li | Changed intensity ratios between the blue, green, and red emission peaks | Hydrothermal | Phase transition from cubic to tetragonal occurs, electron cloud of the ions was distorted [18] |
| **$NaYF_4$** | 20 Yb | 1 Tm | 15 Li | 10 (blue) and 9 (red) | Hydrothermal | Distortion of the local symmetry[19] |
| **$NaYF_4$** | 20 Yb | 1 Ho | 15 Li | 12 (green) and 3 (red) | Hydrothermal | Distortion of the local symmetry[19] |
| **$NaYF_4$** | 20 Yb | 2 Tm | 20 Li | 3 (800 nm) 2 (700 nm) 3 (480 nm ) | Co-thermolysis | Li$^+$ ions may went into interstitial sites, variability of crystal unit cell and NC size, decreased surface-to volume ratio, smaller fraction of surface active ions, exact reason still a subject of debate. [20] |

|  |  |  |  |  |  |  |
|---|---|---|---|---|---|---|
| **Oxides** |  |  |  |  |  |  |
| **$BaTiO_3$** |  | 2 Er | 3 Li | 56 | Sol-gel | Oxygen vacancy generated, distortion of the local asymmetry around $Er^{3+}$, excitation power dependence and decay time increased, reduced OH groups [21] |
| **$BaTiO_3$** | 5 Yb | 1 Er | 7 Li | 22 (550nm) and 11 (green)<br>(from graph) | Sol-gel | Local symmetry of crystal field around $Er^{3+}$ decreased, increased lifetimes of intermediate states of $Er^{3+}$ [22] |
| **$Bi_2Ti_2O_7$** | 3 Yb | 3 Er | 1.5 Li | 14 (from graph) | template assisted | Distortion of the local symmetry around $Er^{3+}$ and reduction of surface defects [23] |
| **$CaSnO_3$** | 8 Yb | 1 Er | 10 Li | 1.5 | Solid-state | Increased doping level of $Yb^{3+}$, change of crystal field around $Er^{3+}$, decrease process: destroyed crystallinity of $CaSnO_3$ [24] |
| **$CeO_2$** |  | 1 Er | 10 Li | 7 (green) 7 (red) from graph | glycine-nitrate gel-combustion | Rise to the creation of defective structure the same as the oxygen vacancies, modification of the local lattice field around $Er^{3+}$ and lower its local symmetry, increased luminescence lifetimes, ceramics defects, such as pores, grain boundary and grain defects, reduced remarkably [25] |
| **$Gd_2O_3$** | 2 Yb | 0.3 Ho | 20 Li | 3.5 (from graph) | solution combustion | Change in crystal field around the $Ho^{3+}$ ion and reduction in quenching centres [26] |
| **$Gd_2O_3$** |  | 0.75 Er | 3 Li | 9.76 (green) and 6.24 (red) | Co-precipitation | Enhanced quenching concentration of $Er^{3+}$ [27] |
| **$Gd_2O_3$** | 10 Yb | 2 Er | 4 Li | 2 | Co-precipitation + annealing at a high T | Shrunk unit cell of $Gd_2O_3$ NCs, generated oxygen vacancies, environment change around the rare earth ion, and decrease of the crystal symmetry around $Er^{3+}$ ions. [28] |
| **$Gd_2O_3$** |  | 1 Er | 10 Li | 3.3 | Co-precipitation | Distortion of local symmetry around $Er^{3+}$ and enhanced crystallinity [29] |
| **$Gd_2O_3$** | 2 Yb | 0.5 Ho | 3 Li | 10 (green) and 4 (red) from graph | Sol-gel | Change of local symmetry and structure around $Ho^{3+}$ [30] |
| **$Gd_2O_3$** | 3 Yb | 0.5 Tm | 6 Li | 10 | Reverse micro emulsion | Distortion of the local asymmetry around $Tm^{3+}$, decrease of OH (FTIR) [31] |
| **$Gd_6MoO_{12}$** | 8 Yb | 0.16 Er | 0.35 Li | 2.5 (green and red) (from graph) | high temperature solid-state | Decrease of the local symmetry around $Er^{3+}$ [32] |

| | | | | | | |
|---|---|---|---|---|---|---|
| **$Gd_6MoO_{12}$** | 10 Yb | 0.2 Er + 0.5 Tm | 20 Li (15 from graph) | some % (blue) 2 (green) 2 (red) from graph | high temperature solid-state | Lowering of the symmetry of crystal around the rare ions [33] |
| **$Lu_2O_3$** | 2 Yb | 0.5 Tm | 7 Li | 4 (490 and 653nm) | Sol-gel | Modification of the local field symmetry around the $Tm^{3+}$ ion, reduced number of $OH^-$ groups, and enlarged nanocrystal size [34] |
| **$TiO_2$** | 10 Yb | 1 Er | 20 Li | 80 (green) 350 (red) | Sol-gel | Lowered crystal field symmetry [35] |
| **$TiO_2$** | 10 Yb | 1 Er | 10/20 Li | No quantification | Sol-gel | Energy migration between $Er^{3+}$ and $Yb^{3+}$, distortion of crystal field symmetry of $Er^{3+}$ (low $Li^+$ ion concentration), phase transformation (higher $Li^+$ concentration [36] |
| **$TiO_2$** | | 0.1 Er | 2 Li | 110 (green) and 160 (red) | non-aqueous sol–gel | Decrease of crystal field symmetry of $Er^{3+}$ [37] |
| **$Y_3Al_5O_{12}$** | | 1 Er | 13 Li | 36 (green) 23 (red) | Sol-gel combustion | Increased lifetime of $^4I_{11/2}$ level, increased ratio of radiation rate in green emission and increased absorptivity at 980 nm.[38] |
| **$Y_3Al_5O_{12}$** | | 1 Er | 7 Li | 4.6 (green) and 3.5 (red) | Sol-gel combustion | Distortion of local crystal field around $Er^{3+}$, decrease in the amount of $CO_3^{2-}$ and $OH^-$ groups [39] |
| **$Y_2O_3$** | 4 Yb | 1 Ho | 3 Li | 10 (green) and 4 (red) | Citric acid sol-gel | Modification of the local symmetry of the $Ho^{3+}$ ion, reduced number of OH groups [40] |
| **$Y_2O_3$** | | 2 Er | 5 Li | 80 (green) red not analysed | Combustion | Tailoring of $Er^{3+}$ ions' local environment, increased ground state absorption cross section of $Er^{3+}$ ions (theoretical investigations) [41] |
| **$Y_2O_3$** | | 1 Er | 5 Li | 55-90 | Sol-gel | Tailored lifetime of the $^4S_{3/2}$ and $^4I_{11/2}$ states, tailored local crystal field around $Er^{3+}$ ions (theoretical calculations [42] |
| **$Y_2O_3$** | 3.5 Yb | 0.3 Tm + 0.5 Er | 2 Li | 3.4 (blue) 2.9 (green) and 2.5 (red) | Sol-gel | Expected: Modified local symmetry around the RE ions, reduced number of OH group [43] |
| **$Y_2O_3$** | | 2 Er | 3 Li | 20 | Complex precursor (sol-gel) | Modification of the local symmetry of the $Er^{3+}$ ion -> increase of the intra-4f transitions of $Er^{3+}$ ion, and of the homogeneous distribution of $Er^{3+}$ [44] |
| **$Y_2O_3$** | | 0.2 Er | 5 Li and 5Li + 2.5 Zn | 11 and 28 | Sol-gel | Increased lifetime of the intermediate state $^4I_{11/2}$ (Er), reduction of defects (OH group) of the nanocrystals [45] |
| **$Y_2O_3$** | 3 Yb | 0.3 Er | 5 Li | 3 | Solution combustion | Decreased unit cell parameter, increased particle size, and removed quenching centres (like OH, NOx, etc.) [46] |

| | | | | | | |
|---|---|---|---|---|---|---|
| **$Y_2O_3$** | 10 Yb | 2 Ho | 5 Li | 8% | Solution combustion | Li+ decreases unit cell parameter of $Y_2O_3$ cubic lattice, increases the particle size, and removes the quenching centres (like OH, NOx, etc.) [47] |
| **$Y_2O_3$** | 3 Yb | 0.1 Tb | 2 Li | 100% | Combustion | Reduction of OH and CO groups (FTIR spectra) [48] |
| **$Y_2O_3$** | 2 Yb | 1 Er | 5 Li | 33 (390/409 nm) and 24 (green) | complex precursor [83] | Prolonged lifetimes of their intermediate states [49] |
| **$Y_2O_3$** | 7 Yb | 4 Er | 1.5 Li | 8 (red) and 4 (green) | Solvent evaporation | Destroyed inversion symmetry and hence the electric-dipole transitions of $Er^{3+}$ become partially allowed, Yb–Er distance changed [50] |
| **$Y_2O_3$** | 2 Yb | 1 Er | 5 Li | 6 (red) and 25 (green) | complex precursor[84] | Tailored local crystal field of the $Y_2O_3$ host lattice, tailoring effect (theoretical calculations) -> increase of lifetimes in the intermediate $^4I_{11/2}$ (Er) and $^2F_{5/2}$ (Yb) states, increase of optically active sites in the $Y_2O_3$ host lattice, and dissociation of the $Yb^{3+}$ and $Er^{3+}$ ion clusters in the nanocrystals [51] |
| **$Y_2O_3$** | 5 Yb | 0.25 Tm | 5 Li | 14 (811 nm) | Sol-gel | Decrease of the local symmetry around $Tm^{3+}$ ions, reduced OH groups, dissociation the $Yb^{3+}$ and $Tm^{3+}$ ion clusters, and creation of oxygen vacancies [52] |
| **$Y_2SiO_3$** | | 1.2 Pr | 5 Li | 9 | Sol-gel decomposition | Crystallite enlargement, ∼50% due to a change in the host crystal polymorph, and ∼45% due to a reduction in activator ion clustering, no significant up-conversion enhancement from activator site geometry change due to distortion [53] |
| **$Y_2Ti_2O_7$** | 7.5 Yb | 1 Er | 10 Li | 18.6 (green) and 8.3 (red) | Citric acid sol-gel | Modification of local symmetry around $Er^{3+}$ ions [54] |
| **ZnO** | | 2 Er | 3 Li | 3.5 (green) 6 (red) (from graph) | Chemical combustion | modification of local crystal field around $Er^{3+}$ ions [55] |
| **$Zn_2SiO_4$** | 3 Yb | 0.5 Er | 1 Li | 6 (green) 3 (red) | microwave processing | Local distortion of $Er^{3+}$, increasing the intra-4f transitions of $Er^{3+}$ ions (proved by spectral probing method with $Eu^{3+}$ [56] |
| **$ZrO_2$** | 12 Yb | 0.5 Er | 0.5 Li | 1.93 (green) and 1.65 (red) | Sol-gel | Tailored local structure of host lattice and improvement of energy transfer processes from $Yb^{3+}$ to $Er^{3+}$, respectively. [57] |
| **$ZrO_2$** | 12 Yb | 0.5 Er | 0.5 Li | 1.65 (green) | Sol-gel | Asymmetry of local environment around RE ions, neutralization of OH groups at the surface of particles [58] |
| **$MO_4$ (M=Mo, P, V, W)** | | | | | | |

| | | | | | | |
|---|---|---|---|---|---|---|
| **$CaMoO_4$** | 8 Yb | 0.5 Tm | 5 Li | 10 | Complex-citrate gel | Break and distortion of crystal field around $TmO_8$ [85] |
| **$CaMoO_4$** | 8 Yb | 2 Er | 10 Li | 83 green | Complex-citrate gel | Local crystal field distortion or break around $Er^{3+}$ ions [59] |
| **$CaWO_4$** | 5 Yb | 10 Er | 5 Li | enhanced (green) but not mentioned | Solid-state | [60] |
| **$CaWO_4$** | 10 Yb | 5 Er | 15 Li | 12 (515 nm) and 7 (540 nm) | Solid-state | [61] |
| **$CaWO_4$, $CaMoO_4$** | 10 Yb | 5 Er | 15 Li | 2-3 | Solid-state | Change of lattice constant and modification of local crystal field symmetry around RE ion [62] |
| **$GdVO_4$** | 20 Yb | 1 Ho | 10 Li | 2.2 | high temperature solid-state | Flux for crystallization, no change in the crystallite size observed, Altering of the local crystal field, or symmetry, of rare earth ions, break of rare earth ion pairings, and creation of oxygen vacancies [63] |
| **$GdVO_4$** | 20 Yb | 1.5 Er | 5 Li | 4 | Solid-state | Breakage of $Yb^{3+}$ ion pairing [64] |
| **$GdVO_4$** | ? Yb | ? Ho and Tm | 8wt% Li | 6 blue and 4 green; 4 NIR | Sol-gel | Increase in the lifetimes of the associated energy levels [65] |
| **$NaZnPO_4$** | 1 Yb | 0.3 Er | 1 Li | 3 (green) and 1.6 (red) | Solid-state | Efficient energy transfer from $Yb^{3+}$ to $Er^{3+}$ and modification in the local field around the RE ions. [66] |
| **$SrWO_4$, $SrMoO_4$** | 10 Yb | 5 Er | 15 Li | 4-10 | Solid-state | Change of lattice constant and modification of local crystal field symmetry around RE ion [62] |
| **$YMoO_4$** | 4 Yb | 0.5 Ho | 2 Li | 104 (green) and 160 (red) | Co-precipitation | Modified local crystal field around the rare earth ions [67] |
| **$ZnWO_4$** | Yb | Er | Li | Red shift | liquid-phase sintering | Lowering of the local symmetry of the crystal field around $Er^{3+}$ [68] |

**Glasses**

| | | | | | | |
|---|---|---|---|---|---|---|
| **$SiO_2$-$Al_2O_3$-$ZnF_2$-$SrF_2$** | | 1 Er | 1.5 Li | >10 | melting and quenching | Charge compensation as well as modification of the local crystal field around the $Er^{3+}$ ions.[69] |

This review focus on the effect of $Li^+$ ion doping on UC nanoparticles for different host matrices, and its explanation by different research groups. Summarising, doping of $Li^+$ ions up to a certain concentration in lanthanide doped nanocrystals enhances the UC emission. A common explanation for the UC emission enhancement is the distortion of the crystal lattice around the trivalent lanthanide ions caused by the incorporation of $Li^+$ on either substitutional cation sites, or on interstitial sites due to its small ionic radius. [18, 19, 21-26, 28-37, 39-44, 50-59, 62, 63, 66-69, 82, 85-91] With increasing $Li^+$ ion concentration, it is assumed that the possibility of occupation of interstitial sites increases. In some hosts, even the phase and crystal structure can change, which is expected to have an effect on the site occupancy of lanthanide ions. [18, 36] In addition, the increased crystallinity and the particle/crystallite size due to $Li^+$ doing is explained by the lower melting temperature of Li precursors whereby $Li^+$ ions can act as a flux. [20, 29, 34, 46, 47, 63, 81] Moreover, it is often stated that $Li^+$ ions decrease the amount of quenching centres ($OH^-$, $CO_2^{3-}$, etc.) on the surface of the nanoparticles, increasing UC emission by decreasing non-radiative transitions. [16, 21, 31, 34, 39, 40, 43, 45-48, 52, 58] In addition, it has been proposed that $Li^+$ can act as a charge compensating ion when trivalent lanthanide ions replace non-trivalent cation sites. [30, 69] Another explanation for the UC enhancement is an increased lifetime of intermediate levels of activator ions. [17, 22, 25, 38, 42, 45, 49, 51, 65] In addition it is also assumed that doping of $Li^+$ can lead to changes in separation between the ions which influences the energy transfer processes and therefore the UC efficiency. Shifts in the emission spectra, especially blue shift, are also observed enabling colour tuning for targeted applications. [17, 30, 69] However, there is a lack of chemical analysis to prove the effective incorporation of $Li^+$ ions in the lattice. (Only by references [54, 87, 91]) However, quantitative analysis and experimental details for the enhancement of the $Ln^{3+}$ emissions by $Li^+$ ion doping have been overlooked. The relative emission intensity (in arbitrary units) of different samples is usually reported and used as emission efficiency comparison, which leads to erroneous conclusion as the emission intensity is sensitive and strongly depends on the measurement conditions (e.g., sample volume and optical setup) even for the same sample and absorption cross-section. Therefore, this project aims at investigating the effect of $Li^+$ on the upconversion emission efficiency of $Y_2O_3$: $Yb^{3+}/Er^{3+}$ nanoparticles and at quantifying the corresponding up-conversion enhancement/efficiency by measuring the emission quantum yields and emission spectral flux. $Y_2O_3$ is used as a host as it is biocompatible; it has a high mechanical and chemical durability, high thermal stability and excellent optical properties. [76] The couple of $Er^{3+}$ and $Yb^{3+}$ is at the centre of up-conversion research because these ions possess suitable properties. While the activator $Er^{3+}$ has a long live and well separated intermediate energy levels, which limit non-radiative energy transfers, the sensitizer $Yb^{3+}$ has a high absorption cross-section at 980 nm and allows an efficient energy transfer to $Er^{3+}$. [76]

The methods used here are radiant flux measurements using an integrating sphere, (scanning) transmission electron microscopy ((S)TEM), Fourier transform infrared spectroscopy (FTIR), thermogravimetric analysis (TGA), Inductively coupled plasma atomic emission spectroscopy (ICP-AES), x-ray photoelectron spectroscopy (XPS) and powder x-ray diffraction (XRD).

# 2 Theory

## 2.1 X-Ray Diffraction and Scherrer's Equation

Powder x-ray diffraction (XRD) is a technique to analyse the types (and quantities) of phases present in a sample including the crystal structure, crystalline size and the unit cell parameter. X-rays interact with the electron clouds of the sample and are scattered depending of the arrangement of the atoms in the sample described by the Bragg's law (1). It gives the condition for constructive interference in the case when the path difference between two diffracted beams is a multiple integer of the wavelength and therefore the condition for diffraction signals of lattice planes. [92]

$$n\lambda = 2d_{hkl}sin\theta \tag{1}$$

where n is an integer, λ is the wavelength, $d_{hkl}$ is the distance between two lattice planes described by the Miller indices hkl and θ the Bragg angle.

The Rietveld method is used to analyse powder diffraction data by simultaneous refining the full pattern profile by the use of known crystal structures or models minimizing the difference between the overall measured and calculated intensities of diffraction patterns. [92]

A correlation between the broadening of the peaks in the XRD patterns and the average crystallite size d is given by the Scherrer's equation (2):

$$d = \frac{0.89\lambda}{\beta cos\theta} \tag{2}$$

where λ is the wavelength of the x-ray radiation, β is the full width at half maximum (FWHM) and θ is diffraction angle. The error for the crystallite size is given by equation (3).

$$\delta d = d\sqrt{\left(\frac{d\beta}{\beta}\right)^2 + (tan\,\theta\delta\theta)^2} \tag{3}$$

## 2.2 Transmission Electron Microscopy

Transmission electron microscopy (TEM) is used to analyse the morphology and structure of a sample. In conventional light microscopes using photons to obtain images, the resolution is given by the Rayleigh criterion (3) which gives a resolution of around 300 nm for green light.

$$\delta = \frac{1.61\lambda}{\mu sin\beta} \tag{4}$$

where $\delta$ is the smallest resolvable distance, $\beta$ the semi-angle of the magnifying lens and $\mu$ the refractive index of the viewing medium. Electron microscopes use electrons to obtain an image whose wavelength λ can be changed by their energy E. This relationship is described by Louis de Broglie's equation (3). Taking this equation, a theoretical resolution of around 4 pm could be achieved for a 100 keV electron. However the resolution of TEMs is restricted to around 0.1 Å by the quality of electron lenses. [93]

$$\lambda = \frac{1.22}{\sqrt{E}} \tag{5}$$

In a TEM electrons are emitted in an electron gun, condenser lenses vary the illumination area of the sample and the transmitted electrons are guided to a fluorescent screen where the electron-intensity distribution is imaged. To record the image, the fluorescent screen can be coupled to a CCD camera or directly exposed photographic emulsion or image plates can be used. The samples need to be prepared as thin as possible, typically 5-100 nm, to avoid an excessive interaction by elastic and inelastic scattering of electrons with the atoms of the sample. Therefore the adequate sample preparation is crucial for good images. In scanning electron microscopy (STEM) an additional condenser-lens is needed which enables a scanning of the sample. This leads to the advantages that thicker specimens and secondary electrons as well as backscattered electrons can be recorded. Selected-area electron diffraction (SAED) is a technique integrated in the TEM that gives information about crystal orientation and structure of an area with a dimeter of 0.1-1 µm at the same spot which is regarded in the image mode. [94]

## 2.3 Inductively Coupled Plasma Atomic Emission Spectroscopy

Inductively coupled plasma atomic emission spectroscopy (ICP-AES), sometimes called inductively coupled plasma optical emission spectrometry (ICP-OES) is a technique used to analyse the chemical composition of up to 40 elements with a detection limit in the range of parts per billion (ppb). With an ICP torch the sample is atomised and excited by producing a plasma. Due to transitions of excited states to the ground state or states with lower energy, an elemental specific electromagnetic radiation is emitted. The radiation is separated by a scanning monochromator or suitable polychromators and detected. Using a reference, a quantitative relative elemental composition can be obtained. [95]

## 2.4 Fourier Transform Infrared Spectroscopy

Fourier transform infrared spectroscopy (FTIR) studies the interaction of IR radiation with matter. A spectrum is obtained by the irradiation of the sample with IR radiation and detection of the absorbance. The absorbance, A, is related to the molecule concentration c in the sample by the Lambert-Beer's law (6)

$$A = \varepsilon l c \tag{6}$$

where ε is the absorptivity and l is the path length. Therefore the height or area of the peaks in an absorbance spectrum are used to determine the concentration of molecules in the sample. By convention, the x-axis of IR spectra is plotted inversed from high to low wavenumbers. In contrast to a dispersive spectrometer, which measures intensity in a narrow range of wavelength, an FTIR spectrometer simultaneously collects data over a wide spectral range which enables shorter measurement times. [96]

## 2.5 Thermogravimetric Analysis

Thermogravimetric analysis (TGA) is a technique used to measure the weight loss of a sample with increasing temperature and constant heating rate or as a function of time with a constant temperature whereby physicochemical properties can be deduced. For example, TGA can provide information about second-order phase transitions, including vaporization, sublimation, absorption and desorption, as well as chemisorption, desolvation (especially dehydration), and decomposition. [97]

## 2.6 X-ray Photoelectron Spectroscopy

X-ray photoelectron spectroscopy (XPS) is a surface specific technique that gives a direct indication about the binding energy of the elements present in the sample. In XPS, the sample surface is irradiated with photons, usually $Mg_{K\alpha}$ radiation, which excite core electrons of the atoms in the sample which lead to ionization of the sample and the emission of a photoelectron with an approximate kinetic energy equal to the difference between the energy of the photon energy and the binding energy. The kinetic energy of the photoelectrons is inversely proportional to the binding energy. The matrix and the kinetic energy of the photoelectron determine the attenuation length which limit the information depth to the nanometre region. [98]

## 2.7 Up-Conversion

Lanthanide-doped up-conversion nanoparticles have the ability to combine two or more photons to generate a single photon with higher energy by an anti-Stokes process.[10] This process of creating a photon with higher energy than the incoming photons is called up-conversion. Figure 5 depicts the ideal up-conversion process for the couple $Yb^{3+}$ and $Er^{3+}$ which is used in up-conversion nanoparticles in this project. $Yb^{3+}$ absorbs radiation and an electron from the $^{2}F_{7/2}$ electronic state is excited to the $^{2}F_{5/2}$ level. By an energy transfer (ET) mechanism an electron of the $Er^{3+}$ ion in the $^{4}I_{15/2}$ state is excited to the $^{4}I_{11/2}$ level. By another incoming photon this electron is further excited to the $^{4}F_{7/2}$ state and by a non-radiative de-excitation it is converted to the $^{4}S_{3/2}$ state. By de-excitation to the ground state $^{4}I_{15/2}$ of $Er^{3+}$ a photon with a higher energy than the incoming photons is emitted.

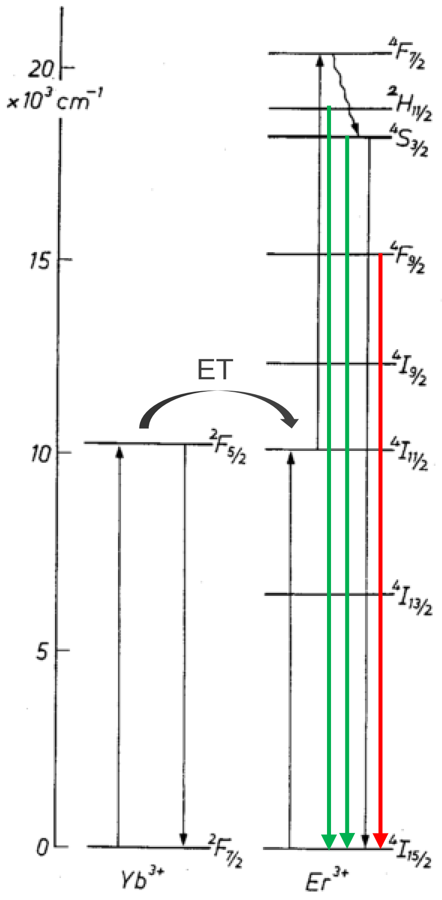

Figure 5: Scheme of the up-conversion process for the couple $Yb^{3+}/Er^{3+}$. Bold arrows depict radiative and corrugated arrows non-radiative transitions. The up-conversion process contains an energy transfer (ET) from the $Yb^{3+}$ ion to the $Er^{3+}$ ion. [99]

Other pathways lead to different wavelength of the emitted photons. Both de-excitation of electrons in the $^{2}H_{11/2}$ and $^{4}S_{3/2}$ states to the ground state $^{4}I_{15/2}$ lead to emission of a photon in the green range with a wavelength of 525 nm and 542 nm, respectively. A transition from the $^{4}F_{9/2}$ electronic state to the ground state $^{4}I_{15/2}$ provokes the emission of a photon with the wavelength of 655 nm in the red range of the visible light. [100]

Figure 6, [101] depicts the up-conversion mechanisms in more detail for the Er$^{3+}$, Yb$^{3+}$ couple upon 980 nm excitation. Either the $^{2}F_{5/2}$ state of Yb$^{3+}$ is excited from its ground state $^{2}F_{7/2}$ with an energy transfer mechanism exciting the $^{4}I_{11/2}$ state of Er$^{3}$, or Er$^{3+}$ absorbs the energy directly. An excited electron in the $^{4}I_{11/2}$ state may:

1. De-excite to the $^{4}I_{13/2}$ state and by the absorption of another excitation photon of 980 nm the $^{4}F_{9/2}$ will be excited if the excess energy can be absorbed by phonon scattering. By de-excitation of the $^{4}F_{9/2}$ to the ground state a red photon is emitted.
2. Cross-relax with an excited electron in the $^{4}F_{7/2}$ which leads to two electrons in the $^{4}F_{9/2}$. De-excitation to the ground state leads to the emission of a red photon.
3. It can be further excited by a photon of the laser source, leading to excited state absorption (ESA). Therefore the $^{4}F_{7/2}$ state is occupied and converted by non-radiative de-excitation to the $^{2}H_{11/2}$ or $^{4}S_{3/2}$ state. De-excitation of these states lead to green emission with a wavelength of 525 nm and 542 nm, respectively.

Another pathway is a cross-relaxation mechanisms of $^{2}H_{11/2}$ + $^{4}I_{15/2} \rightarrow$ $^{4}I_{9/2}$ + $^{4}I_{13/2}$ which increases with higher concentrations of Er$^{3+}$ and causes significant depopulation of the upper excited states. [102]

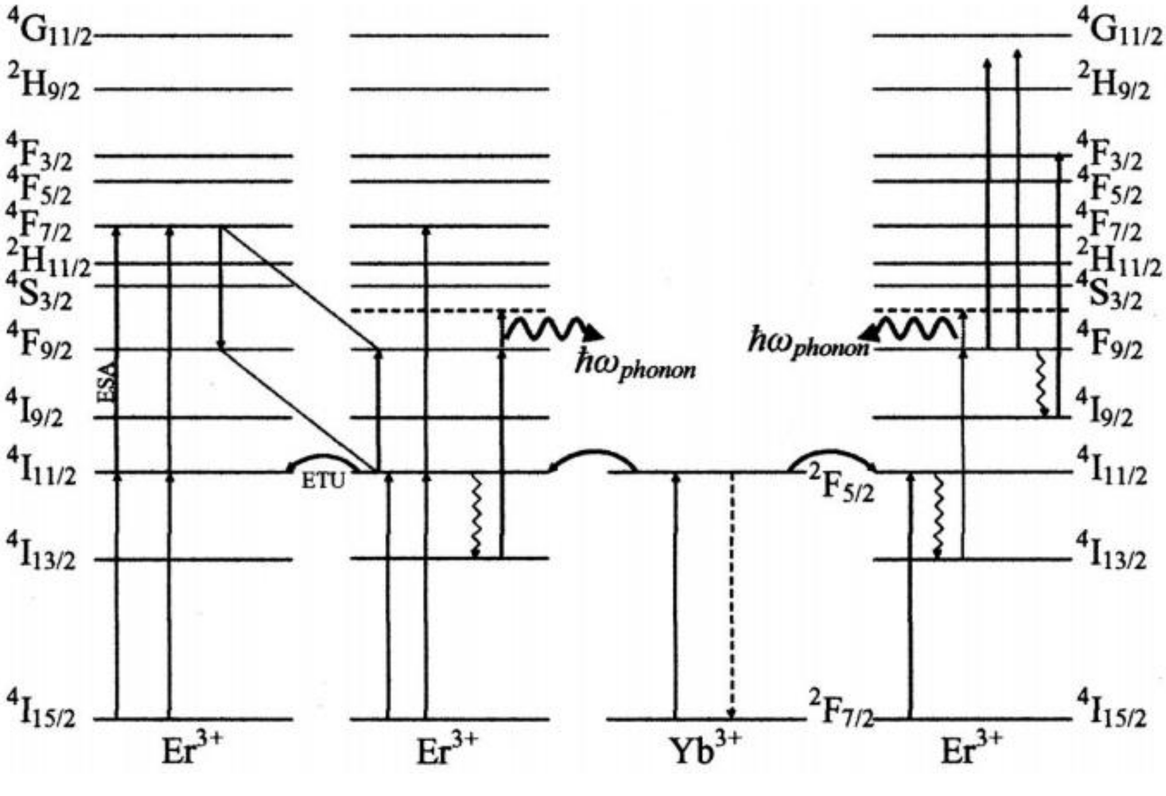

Figure 6: Schematic of up-conversion mechanisms for the couple Er$^{3+}$ and Yb$^{3+}$ under excitation of 980 nm, taken from ref. [101]

## 2.8 Photoluminescence Spectroscopy and Emission Quantum Yield

Figure 7 depicts the scheme of the setup of an integrating sphere proposed in ref.[103]. A customized optical fibre guides the excitation radiation to the sample holder illuminating the sample in form of a powder or in solution. The emitted radiation is collected by the ISP-150L integrating sphere and then guided through an optical fibre to the CCD camera of the MAS-40 detector, that quantifies the spectral radiant flux S as a function of the wavelength λ. In contrast to a conventional luminescence measurement the emitted radiation can be related to the incoming radiation.

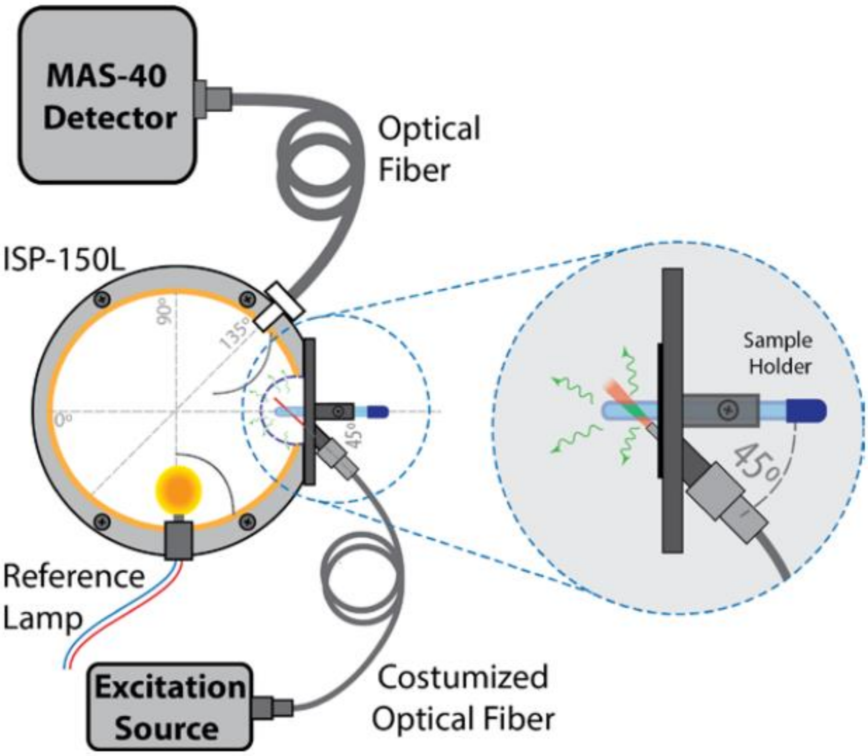

Figure 7: Scheme of the experimental setup for measuring the radiant flux using an integrating sphere taken from ref.[103]

This relationship is described by the emission quantum yield, q, which is defined by equation (7)

$$q = \frac{N_e}{N_a} \tag{7}$$

which requires an independent quantification of the emitted photons $N_e$ and absorbed photons $N_a$. This can be done by the following steps. The spectral radiant flux S as a function of the photon wavelength λ in the visible spectral range is quantified by an integrating sphere connected to a CCD camera and is given by equation (8)

$$S(\lambda) = \frac{dP}{d\lambda} = \frac{d}{d\lambda}\left(\frac{dN}{dt}\frac{hc}{\lambda}\right) = \frac{hc}{\lambda}\frac{d}{d\lambda}\left(\frac{dN}{dt}\right) \tag{8}$$

where c is the speed of light in vacuum, h is the Planck constant and dN/dt is the photon flux per unit of time. The power P is given by the product of the number of photons by its energy. Therefore, the number of photons N ($N_e$ or $N_a$) is determined from the experimental measurement of S(λ) by equation (9)

$$\frac{dN}{dt} = \frac{1}{hc}\int_{\lambda_{min}}^{\lambda_{max}} [S(\lambda)\lambda] d\lambda \tag{9}$$

where the integral limits correspond to the emission ($N$=$N_e$) or absorption ($N$=$N_a$) spectral ranges. Experimentally, $N_a$ is the difference between the number of photons not absorbed by the sample and the reference, which is an empty sample holder for powders or a solvent filled sample holder for suspensions. [104, 105] If the excitation wavelength lays outside the CCD camera responsivity limits (370- 808 nm) an additional detection system is required to quantify $N_a$. This is the case of the $Li^+$ doped $Y_2O_3$: $Yb^{3+}$/$Er^{3+}$ nanoparticles excited at 980 nm. In this particular case, $N_a$ will be quantified by equation (10)

$$\frac{dN_a}{dt} = \frac{P\lambda}{hc} \tag{10}$$

where the power $P$ is measured using a power meter device which is able to accurately quantify $N_a$ in the NIR range between 808 nm and 980 nm. [106] The quantum yield can be quantified by combining equations (7), (9) and (10) to equation (11).

$$q = \frac{\int_{\lambda_{min}}^{\lambda_{max}} [S(\lambda)\lambda] d\lambda}{P\lambda} \tag{11}$$

The corresponding error $\Delta q$ is given by equation (12).

$$\begin{aligned}(\Delta q)^2 &= \left(\frac{\partial q}{\partial P}\Delta P\right)^2 + \left(\frac{\partial q}{\partial \lambda}\Delta\lambda\right)^2 + \left(\frac{\partial q}{\partial S}\Delta S\right)^2 \\ &= \frac{1}{(P\lambda)^2}\left(-\int [S(\lambda)\lambda] d\lambda \frac{\Delta P}{\mathrm{P}}\right)^2 + \left(\left(S(\lambda)\lambda^2 - \int [S(\lambda)\lambda] d\lambda\right)\frac{\Delta\lambda}{\lambda}\right)^2 + \left(\left(\int \lambda d\lambda\right)\Delta S\right)^2\end{aligned} \tag{12}$$

in which $\Delta S/S$ equals 0.10, according to the manufacturer, the emission spectra resolution $\Delta\lambda$ is 0.1 nm, and $\Delta P/P$ is 0.05.

Under the condition of direct illumination, the influence of light scattering on the determination of emission quantum yields is minimized with an integrating sphere with a reduced number of ports and a high-reflective and uniform coating which is the case in this project. [107]

# 3 Experimental

## 3.1 Nanoparticle Synthesis

### 3.1.1 Reflux/Co-Precipitation Method

The nanoparticles were synthesized by modifying the procedure reported in ref. [80]. Briefly, an aqueous solution containing 97-a mol% $Y(NO_3)_3$ (((97-a)/100)x3 ml 0.4 M), 2 mol% $Yb(NO_3)_3$ (0.06 ml, 0.4 M), 1 mol% $Er(NO_3)_3$ (0.120 ml, 0.1 M) and a mol% $LiNO_3$ (2a/100)x3 ml, 0.2 M)) with a=0, 2, 5 or 15, was mixed in a round-bottom-flask. The solution was filled up with 265 ml of distilled water, 2.7 g urea and 0.6 g cetyl trimethylammonium bromide (CTAB) surfactant. After 30 minutes of vigorous stirring and 3 times 1 minute sonification the solution was heated at 86.5 ±3 °C for 2 or 4 hours. Nanoparticles nucleated in the solution, visible by the change of transparency shown in Figure 8.

Figure 8: Nucleated nanoparticles in water solution with urea and CTAB as surfactant.

After cooling naturally to room temperature the nanoparticles were alternatively separated by centrifugation and washed with deionized water and a mixture of 50 % water and ethanol at the end. The nanoparticles were dried in an autoclave at 75 °C for at least 12 hours. In a last step the nanoparticles were calcined from room temperature to 800 °C with a heating rate of 2 °C/minute for 3 hours and grinded afterwards.

### 3.1.2 Sol–Gel Mixing and Solid State Reaction Route

$Y_2O_3$ powders doped ('tri-doped') with $Er^{3+}/Yb^{3+}/Li^{+}$ were synthesized by a sol–gel mixing and solid-state reaction route, a modification of the procedure reported in references [54, 108]. $Y(NO_3)_3$, $Yb(NO_3)_3$, $Er(NO_3)_3$, and $LiNO_3$ were the precursor materials. Hydrous citric acid and absolute ethanol were used as chelator and solvent, respectively. Briefly, an aqueous solution containing 97-a mol% $Y(NO_3)_3$ (((97-a)/100)x5 ml 0.4 M), 2 mol% $Yb(NO_3)_3$ (0.1 ml, 0.4 M), 1 mol% $Er(NO_3)_3$ (0.2 ml, 0.1 M) and a mol% M (M = $LiNO_3$ (2a/100)x5 ml, 0.2 M) with a equal to 0, 1, 2.5, 5 and 10 was mixed under magnetic stirring and ultrasonic treatment, respectively for 15 minutes. The solution was dried in an autoclave at 75 °C for at least 12 hours until the water was completely evaporated and only a dried salt was left. Subsequently, citric acid with a ratio of n (citric acid)/n (Y, Yb, Er, and Li) = 2.5 was dissolved thoroughly in absolute ethanol and the mixture was stirred vigorously until it became a homogeneous transparent solution. The ethanol- citric acid solution was poured into the dried salt. The solution was heated at 80 °C to vaporize excessive solvent, then became highly viscous, and, finally, changed into transparent glassy gel as shown in Figure 9.

Figure 9: Transparent glassy gel of citric acid, ethanol and $Y(NO_3)_3$, $Yb(NO_3)_3$, $Er(NO_3)_3$, and $LiNO_3$ solution.

No visible precipitation was observed during gelation. The xerogel was transferred to a crucible and heat-treated at 800 °C for 1 hour in static air with a heating rate of 5 °C/minute followed by a cooling rate of 5 °C/minute to room temperature. A white powder was obtained, shown in Figure 10, which is grinded

Figure 10: Calcined powder after solid state reaction at 800 °C for 1 hour.

## 3.2 X-Ray Diffraction

The samples were mixed with a Standard Reference Material® 640e (Silicon powder) and powder XRD patterns recorded in the range 16 - 112 °2θ, with a step size of 0.0130°, on a PANalytical Empyrean X-ray diffractometer operating at 45 kV and 40 mA, with $Cu_{K\alpha}$ radiation at 1.5406 Å. The patterns were displaced until the silicon peaks reflections matched the reflections of the silicon reference. Rietveld-refinement was performed using the diffraction patterns of the sample and the reference data of $Y_2O_3$ (04-007-9751) and silicon (04-016-4861) taken from the International Centre for Diffraction Data (ICDD) database.

## 3.3 (Scanning) Transmission Electron Microscopy

The samples were grinded, diluted in water, sonicated and a drop of the solution was transferred to a TEM grid which was dried at least for 12 hours. The nanoparticles were examined by a Hitachi H9000-NA TEM with an acceleration voltage of 300 kV and a Hitachi HD-2700 STEM with an acceleration voltage of 80 and 200 kV. The crystal structure was analysed by selected area electron diffraction (SAED).

## 3.4 Inductively Coupled Plasma Atomic Emission Spectroscopy

The samples were analysed by the Central Laboratory of Analysis (LCA) with an ICP-OES Jobin Yvon Activa M. The LCA is a unit of the University of Aveiro (UA) responsible for the execution and delivery of analytical services requested by internal and external customers of the university.

## 3.5 Fourier Transform Infrared Spectroscopy

IR spectra were recorded on a Bruker FTIR TENSOR 27. For the reflectance mode the powders were measured without further preparation, whereas for the transmission mode, pallets were pressed. Therefor 1.5 mg of each sample was mixed with 200 mg KBr, respectively. The mixtures were grinded, pressed uniaxial with 9 tons for 2 minutes and semi-transparent pallets were obtained. 256 scans were taken for wavenumbers between 350 and 4000 $cm^{-1}$ with a resolution of 4 $cm^{-1}$.

## 3.6 Thermogravimetric Analysis

Between 4 and 15 mg of the samples were analysed by a thermogravimetric analyser TGA-50 from Shimadzu. The samples were heated from room temperature to 800 °C with a rate of 5 °C/minute and the weight loss was measured every second.

## 3.7 X-Ray Photoelectron Spectroscopy

XPS spectrums were acquired in an Ultra High Vacuum (UHV) system with a base pressure of $2x10^{-10}$ mbar located at TEMA, University of Aveiro. Figure 11 depicts the system which is equipped with a hemispherical electron energy analyser (SPECS Phoibos 150), a delay-line detector and a monochromatic $Al_{K\alpha}$ (1486.74 eV) X-ray source. High resolution spectra were recorded at normal emission take-off angle and with a pass-energy of 20 eV, which provides an overall instrumental peak broadening of 0.5 eV. The samples (powder) were suspended in $mQH_2O$ and drop coated on Si wafers. The samples were measured using an electron gun for charge compensation. No binding energy correction was done to these data.

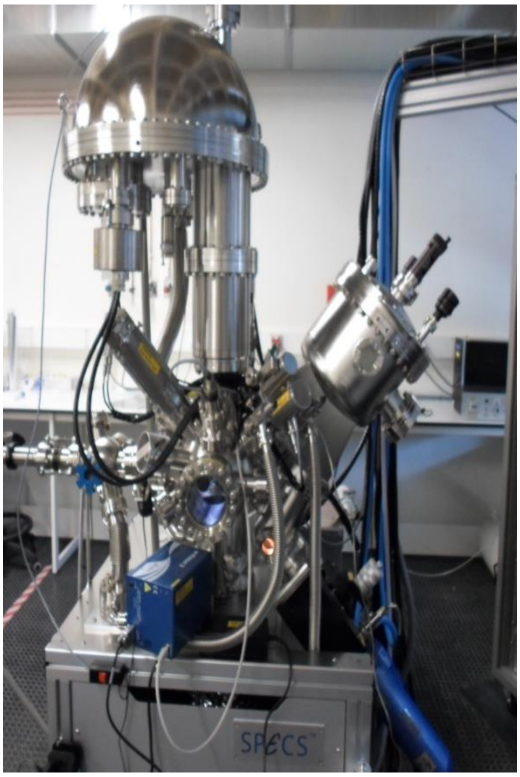

Figure 11: XPS system located at TEMA, University of Aveiro.

## 3.8 Radiant Flux Measurements Using an Integrating Sphere

The emission spectral radiant flux of powder samples was measured using an integrating sphere (ISP 150L-131, Instrument Systems) depicted in Figure 12 with the by Carlos et al [103] proposed schematic setup, shown in Figure 7.

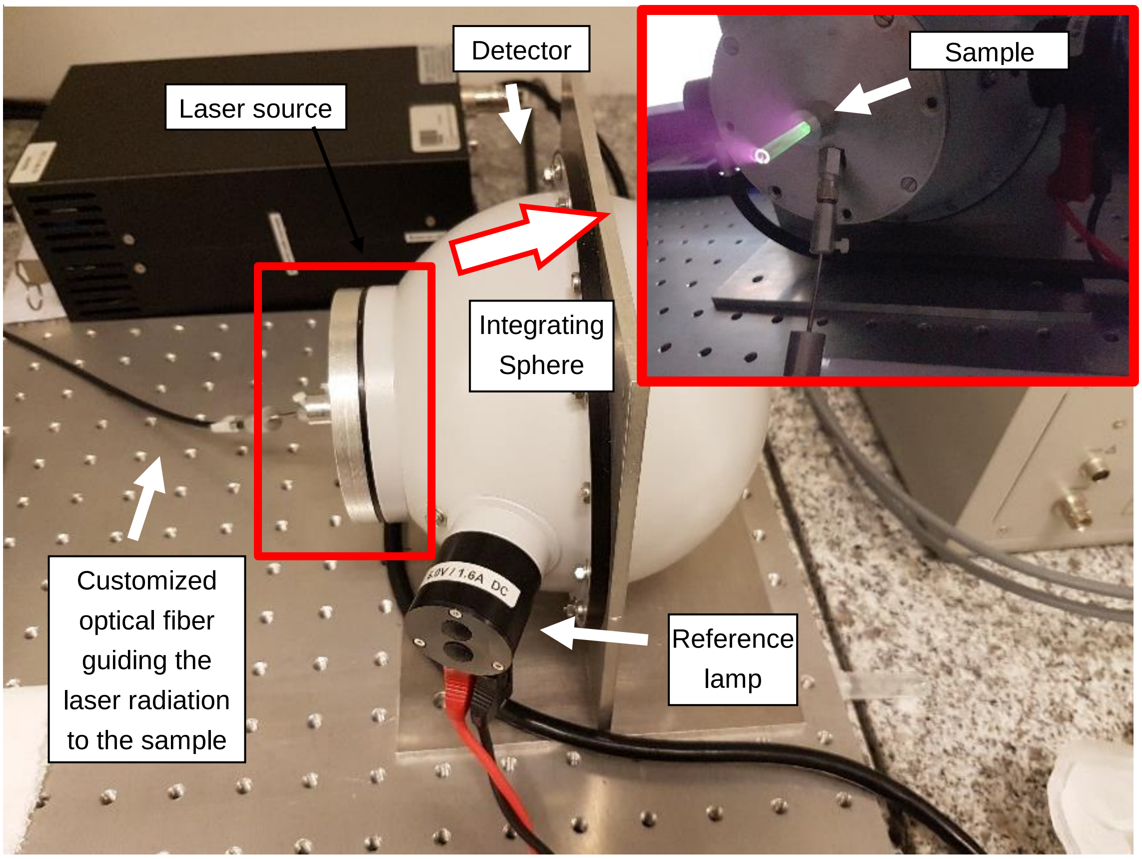

Figure 12: Picture of the integrating sphere setup used in this project with a side view during a measurement inserted in the upper right corner.

All the spectra were acquired with a resolution of 0.5 nm, 20 s integration time and 2 averaged spectra scans in the wavelength range of 500 to 720 nm. The integrating sphere ($BaSO_4$ coating) has an internal diameter of 150 mm and was coupled to an array spectrometer (MAS-40, Instrument Systems). The measurements have an accuracy within 5%, according to the manufacturer. A customized optical fibre (SarSpec, 0.6 mm core diameter with an adaptable-length ferrule) guides a 980 nm CW laser diode (CNI, MDL-H-980 laser controlled by a PSU-H–LED power source). The radiant flux of the samples was measured for laser power densities up to 999 W/cm$^2$. The background was subtracted taking into account the contribution of the reflection coming from the sample holder by recording the respective spectra of an empty sample holder.

# 4 Results & Discussion

## 4.1 Reflux/Co-Precipitation Method

In a first part of the project the synthesis method adapted from ref. [28, 80] was used to synthesize $Li^+$ doped $Y_2O_3$: $Yb^{3+}/Er^{3+}$ nanoparticles. This method has several advantages like spherical particles with tuneable sizes can be produced. The size, structure and chemical composition of the nanoparticles are analysed with XRD, STEM and ICP-AES.

### 4.1.1 X-Ray Diffraction

Figure 13 shows a powder X-ray diffraction (XRD) pattern of $Y_2O_3$: $Yb^{3+}/Er^{3+}$ nanoparticles doped with 2 and 5 mol% $Li^+$ ions. The number of reflections is the same for all patterns and in good agreement with the standard values for the reference data of $Y_2O_3$ (04-007-9751), indicating the samples contain no second crystalline phase.

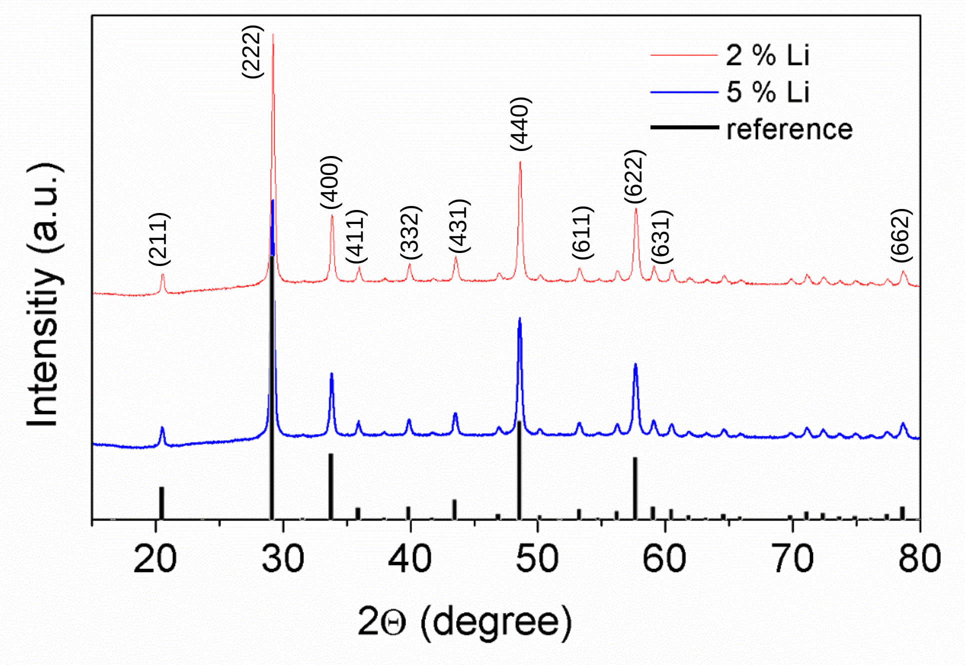

Figure 13: XRD patterns of $Y_2O_3$: $Yb^{3+}/Er^{3+}$ nanoparticles doped with 2 and 5 mol% $Li^+$ ions. The reference data of $Y_2O_3$ (04-007-9751) is depicted as black lines with a relative height corresponding to the relative intensity.

Figure 14 shows the dependence of the lattice parameter obtained by Rietveld-refinement as a function of the $Li^+$ concentration. No error bars are given as no extra measurement with the same sample was done to obtain a statistical error deviation.

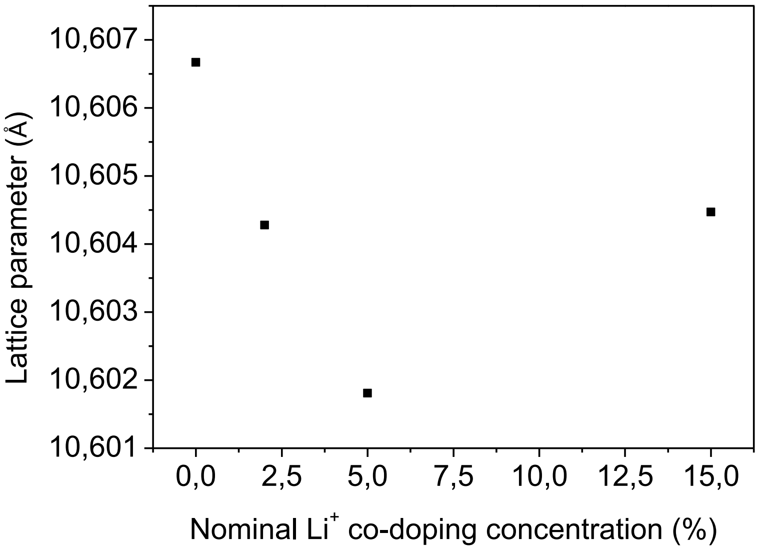

Figure 14: Dependence of the lattice parameter as a function of the nominal Li$^+$ ion doping concentration.

Taking the expected statistical error for such XRD measurement into account (shown in 3.1.2), the resolution of the Rietveld refinement is not high enough to make a conclusion about the incorporation of Li$^+$ ions. Moreover, ICP-AES results reported in section 4.1.3 prove that no Li is incorporated using this method.

Therefore, the explanation given in literature for similar solution based methods [26-29, 31, 67, 86, 88, 109, 110] needs to be checked by analysing the chemical Li content. As in literature no errors are given for the refinement of the powder XRD patterns false conclusions can be made. The predominant argument for the lattice parameter change is the incorporation of Li$^+$ ions at Y$^{3+}$ lattice sites. As the ionic radius of Li$^+$ (90 pm) is much smaller than that of Y$^{3+}$ (104 pm) [73], substitution of Y$^{3+}$ by Li$^+$ would lead to a contraction of the lattice around the ion, decreasing the lattice parameter. This contraction process of the lattice around an incorporated ion is shown in Figure 1 in the scheme for host lattice manipulation as a possible mechanism for the enhancement of luminescent properties of up-conversion nanoparticles. In addition to substitutional crystal sites, Li$^+$ ions may be incorporated into interstitial sites, increasing the lattice parameter. Another option is that the Li$^+$ ions are not incorporated in the crystal which is the case for the co-precipitation method which can be due to the formation of additional crystalline or amorphous phases or the dopant is lost during the synthesis. ICP-AES proves the latter.

### 4.1.2 Scanning Transmission Electron Microscopy

The results of STEM analysis are shown for $Y_2O_3$: Yb$^{3+}$/Er$^{3+}$ nanoparticles doped with 0 and 5 mol% Li$^+$ ions. Figure 15 depicts an example image for $Y_2O_3$: Yb$^{3+}$/Er$^{3+}$ (2/1 mol%)

nanoparticles in b) and the corresponding size distribution in a). The diameter of the nanoparticles obtained by the best log-normal distribution fit of the histogram with centre ± standard deviation σ of $D$=207±30 nm ($r^2$=0.923).

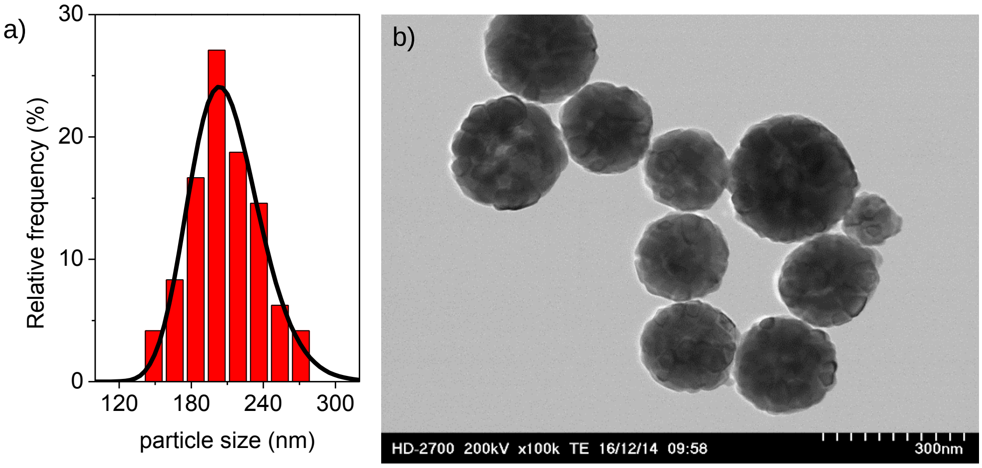

Figure 15: a) Histogram of the particle size distribution of Li-undoped $Y_2O_3$: Yb/Er (2/1 mol%) nanoparticles together with b) an example STEM image. The line in a) is the best fit of the histogram to a log-normal distribution with centre ± standard deviation σ of $D$=207±30 nm ($r^2$=0.923).

Doping the particles with nominal 5 mol% $Li^+$ ions lead to a size decrease and a half pre-reaction time lead to a further size decrease, depicted in Figure 16 and Figure 17, respectively. Again, example images of the nanoparticles are shown in b) and in a) the corresponding size distribution is shown. The diameter of the nanoparticles obtained by the best log-normal distribution fit of the histogram with centre ± standard deviation σ is $D$=162±19 nm ($r^2$=0.919) and decreases to $D$=152±16 nm ($r^2$=0.518) for a half pre-reaction time.

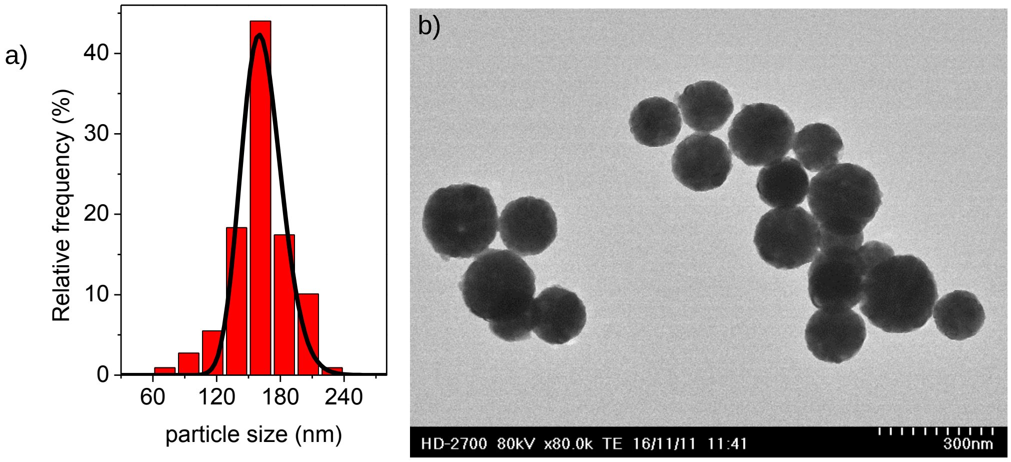

Figure 16: a) Histogram of the particle size distribution for 5 % $Li^+$ ion dopant concentration in $Y_2O_3$: Yb/Er (2/1 mol%) nanoparticles together with b) an example STEM image. The line in a) is the

best fit of the histogram to a log-normal distribution with centre ± standard deviation σ of *D*=162±19 nm ($r^2$=0.919).

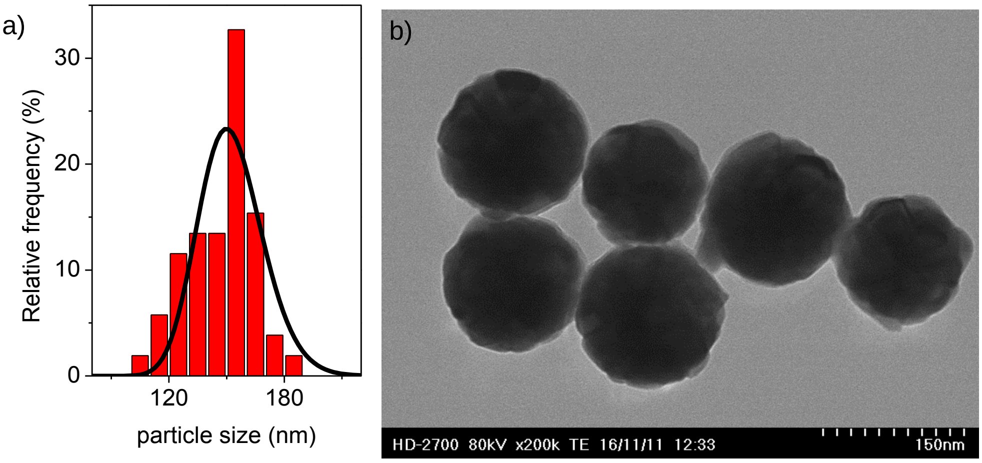

Figure 17: a) Histogram of the particle size distribution for 5 % $Li^+$ ion dopant concentration in $Y_2O_3$: Yb/Er (2/1 mol%) nanoparticles with half pre-reaction time compared to the prior samples together with b) an example STEM image. The line in a) is the best fit of the histogram to a log-normal distribution with centre ± standard deviation σ of *D*=152±16 nm ($r^2$=0.518).

In conclusion the TEM images prove that nanoparticles synthesized by a reflux/co-precipitation method are spherical with sizes larger than 150 nm which can be controlled by the reaction times. Another effect on the size is the temperature of the co-precipitation reaction which is not shown here.

### 4.1.3 Inductively Coupled Plasma Atomic Emission Spectroscopy

The results of the chemical composition obtained by ICP-AES for $Y_2O_3$: $Yb^{3+}/Er^{3+}$ nanoparticles with nominal 5 and 15 mol% $Li^+$, prepared by a reflux/co-precipitation method are shown in Table 2. The nominal $Er^{3+}$ and $Yb^{3+}$ concentrations in both samples are close to the measured concentration. However, no $Li^+$ can be detected. Due to the detection limit of the ICP-AES machine, it can be concluded that less than 0.03 mol% $Li^+$ are present in the samples. This means that the $Li^+$ ions are lost during the synthesis and are not incorporated in the lattice of the nanoparticles.

Table 2: ICP-AES results for ICP-AES for $Y_2O_3$: $Yb^{3+}/Er^{3+}$ nanoparticles doped with $Li^+$ ions prepared by a reflux/co-precipitation method.

| **Concentration** | **Y** mol% | **Er** mol% | **Yb** mol% | **Li** mol% |
|---|---|---|---|---|
| **Nominal** | 92 | 1 | 2 | 5 |
| **Measured** | 96.2 | 1.2 | 2.5 | **0.0** |
| **Nominal** | 82 | 1 | 2 | 15 |
| **Measured** | 96.4 | 1.2 | 2.3 | **0.0** |

It is supposed that the $Li^+$ ions dissolve in the aqueous solution and are removed with the supernatant after the centrifugation step. The reflux/co-precipitation method therefore cannot be used for the synthesis of $Li^+$ ion doped nanoparticles and no further experiments were performed.

However, several research groups use similar solution based methods [26-29, 31, 67, 86, 88, 109, 110] and none checked the actual incorporation of $Li^+$ ions in the sample by analysing the chemical Li content. Discussion of the UC enhancement by $Li^+$ doping reported in the literature, based on the same synthesis therefore are not based on the $Li^+$ incorporation. In the reviewed paper in chapter 1, Li *et al.,* [28] also obtained spherical, monodisperse, crystalline particles with no secondary crystalline phases but they did not check the Li content and therefore their discussion on the UC emissions lacks solid evidence.

## 4.2 Sol–Gel Mixing and Solid State Reaction Route

In the second part of the project another synthesis method was used. Even if the adjusted sol–gel mixing and solid state reaction route proposed by Chen *et al.,* [54, 108] has some drawbacks, *e.g.,* the nanoparticles are not perfectly round, they agglomerate and the size control is more difficult, ICP showed this method allows the $Li^+$ incorporation. Hence, this method was used and the effect of $Li^+$ doping on $Y_2O_3$: $Yb^{3+}/Er^{3+}$ (2/1 mol%) nanoparticles was analysed by XRD, TEM, ICP-AES, FTIR, TGA, XPS and radiant flux measurements using an integrating sphere.

### 4.2.1 Inductively Coupled Plasma Atomic Emission Spectroscopy

Table 3 shows the results of the chemical composition obtained by ICP-AES for $Y_2O_3$: $Yb^{3+}/Er^{3+}$ nanoparticles with nominal $Li^+$ ion doping concentration of 1, 2.5, 5 and 10 mol% prepared by a sol–gel mixing and solid state reaction route. Their actual $Li^+$ content is 0.8, 1.1, 4.8 and 12.3 mol%, respectively. Therefore all samples possess $Li^+$ concentrations which are in accord with the nominal ones except for nominal 2.5 mol% $Li^+$ ions which is less than the half. However, the concentrations of Er and Yb in samples doped with nominal 5 and 10 mol% $Li^+$ are almost twice the nominal concentrations. As a conclusion, the sol–gel mixing and solid-state reaction route leads to the incorporation of $Li^+$ ions in the nanoparticles and therefore these nanoparticles are studied more in detail.

Table 3: ICP-AES results for ICP-AES for $Y_2O_3$: $Yb^{3+}/Er^{3+}$ nanoparticles doped with $Li^+$ ions prepared by a sol-gel route.

| **Concentration** | **Y**<br>**mol%** | **Er**<br>**mol%** | **Yb**<br>**mol%** | **Li**<br>**mol%** |
|---|---|---|---|---|
| **Nominal** | 96 | 1 | 2 | 1 |
| **Measured** | 96.5 | 1.0 | 1.7 | **0.8** |
| **Nominal** | 94.5 | 1 | 2 | 2.5 |
| **Measured** | 96.2 | 0.9 | 1.9 | **1.1** |
| **Nominal** | 92 | 1 | 2 | 5 |
| **Measured** | 89.6 | 1.9 | 3.7 | **4.8** |
| **Nominal** | 87 | 1 | 2 | 10 |
| **Measured** | 82.3 | 1.8 | 3.6 | **12.3** |

### 4.2.2 X-Ray Diffraction

Figure 18 depicts the powder XRD patterns of $Y_2O_3$: $Yb^{3+}/Er^{3+}$ nanoparticles doped with $Li^+$ ions at 0, 0.8, 1.1, 4.8 and 12.3 mol%, and of references $Y_2O_3$ (04-007-9751) and silicon (04-012-7888). As described in section 3.2, a silicon reference is mixed with samples to perform a Rietveld refinement and therefore silicon reflections are present in the patterns. The height of the signal is proportional to the fractions of the mixed powders. No additional peaks are observed, meaning that no extra crystalline phases are present. Scherrer's equation (2) indicates the crystallite size increases with increasing $Li^+$ concentration (Figure 25, depicted in chapter 4.2.3).

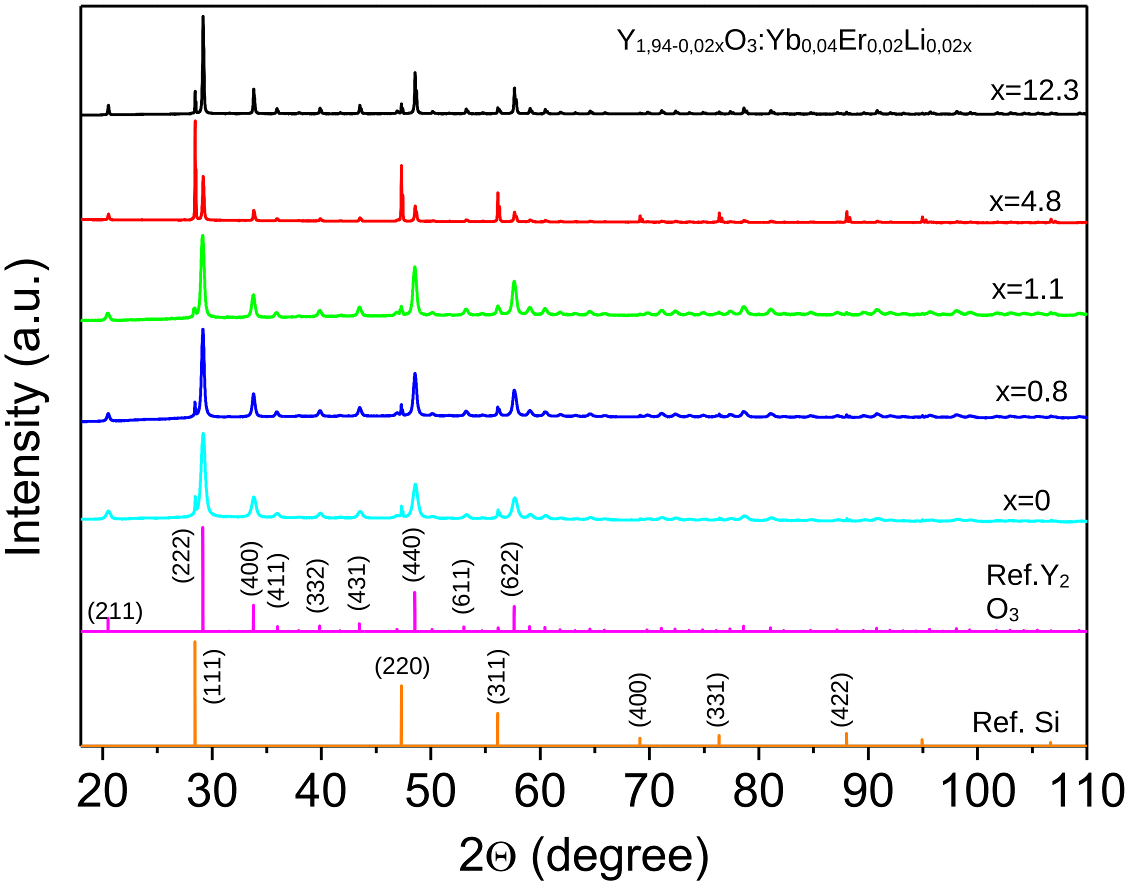

Figure 18: XRD patterns for $Y_2O_3$: $Yb^{3+}$/$Er^{3+}$ nanoparticles doped with the nominal concentration of 0-10 mol% $Li^+$ ions and reference patterns of $Y_2O_3$ (04-007-9751) and silicon (04-012-7888).

Scherrer's equation gives the crystallite size of Li-free $Y_2O_3$: $Yb^{3+}$/$Er^{3+}$ nanoparticles of 19.0±1.3 nm. For 0.8, 1.1, 4.8 and 12.3 mol%, $Li^+$, the crystallite sizes are 33.1±3.7 nm, 31.5±3.3 nm, 77.5±19.7 nm, and 85.9±24.1 nm, respectively. A linear correlation of the crystallite size and the $Li^+$ content is observed which will be explained in detail in the next chapter 4.2.3.

Figure 19 depicts the lattice parameters of $Y_2O_3$: $Yb^{3+}$/$Er^{3+}$ nanoparticles with $Li^+$ concentration 0, 0.8, 1.1, 4.8 and 12.3 mol% obtained by Rietveld refinement. For 12.3 mol% concentration, two measurements with different batches of the same sample were analysed and the error for this measurement is represented. Data points are in the range of the error. Thus, no evidence could be found for interstitial or substitutional incorporation of $Li^+$ ions in the $Y_2O_3$.

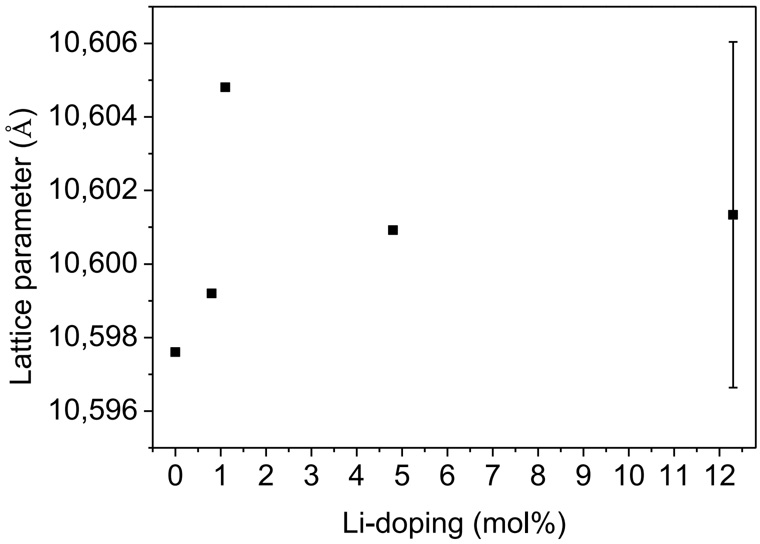

Figure 19: Lattice parameter dependence of the $Li^+$ ion doping concentration determined by Rietveld-refinement.

### 4.2.3 Transmission Electron Microscopy

The morphology of $Y_2O_3$: $Yb^{3+}/Er^{3+}$ (2/1 mol%) nanoparticles was studied by TEM. Figure 20, Figure 21, Figure 22, Figure 23 and Figure 24 depict typical TEM images and histograms of the particle size distribution for 0, 0.8, 1.1, 4.8 and 12.3 mol% $Li^+$, respectively. The nanoparticles are agglomerated and show nearly spherical morphology.

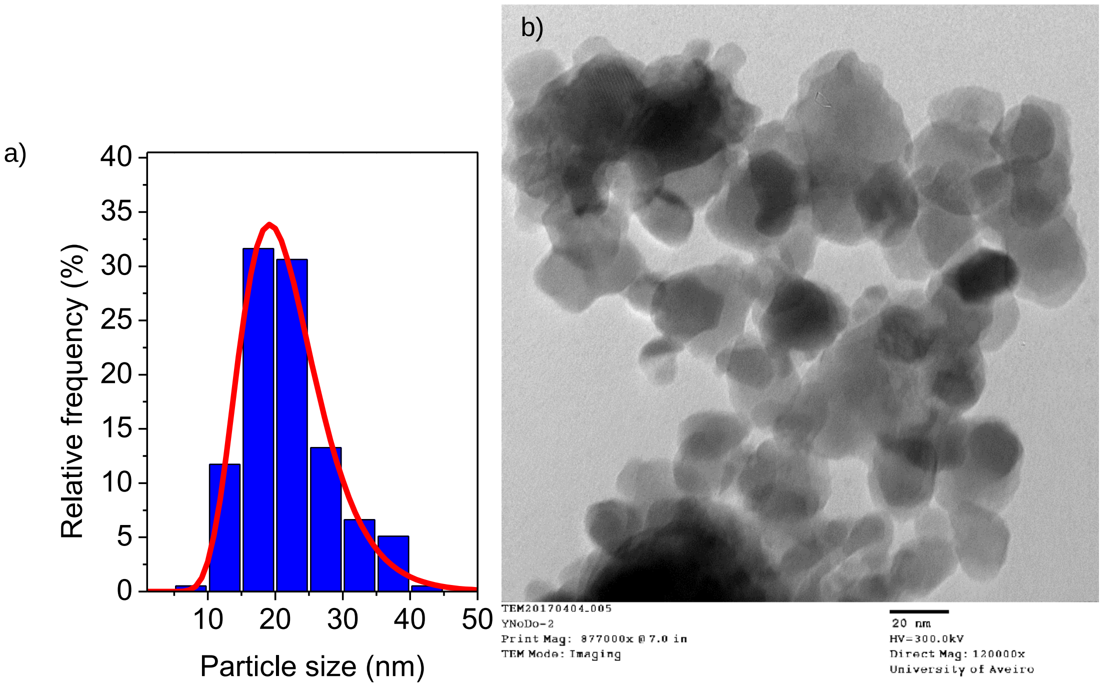

Figure 20: a) Histogram of the particle size distribution of Li-undoped $Y_2O_3$: Yb/Er (2/1 mol%) nanoparticles; b) TEM image. The red line in a) is the best fit of the histogram to a log-normal distribution with centre ± standard deviation σ of *D*=21±5 nm ($r^2$=0.979).

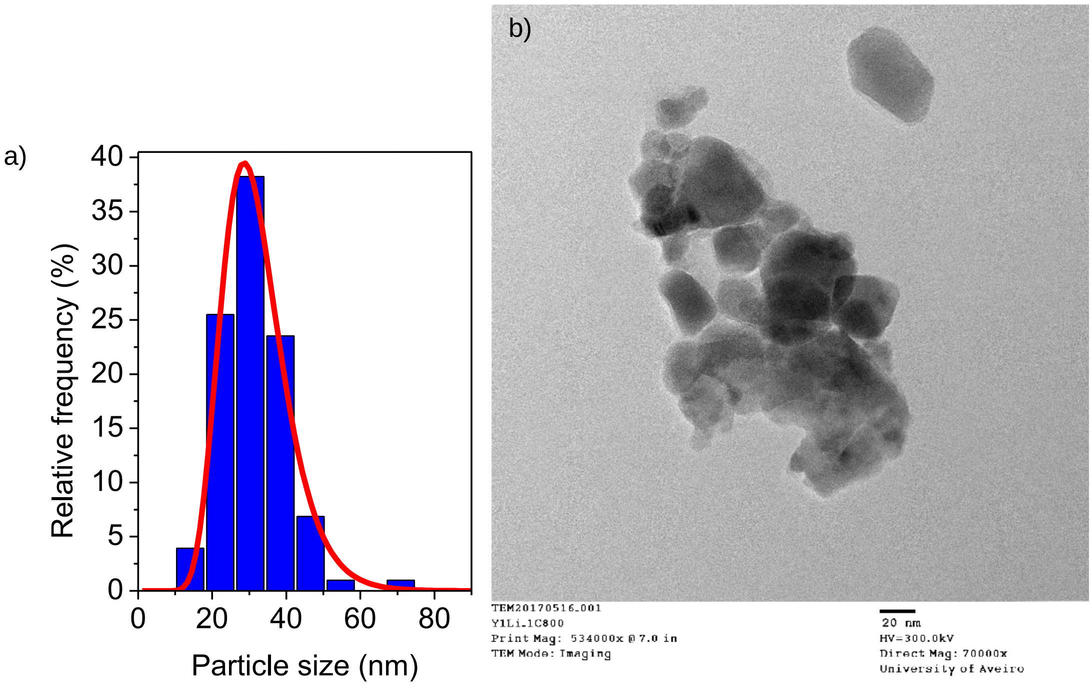

Figure 21: a) Histogram of the particle size distribution for 0.8 mol% $Li^+$ in $Y_2O_3$:Yb/Er (2/1 mol%) nanoparticles; b) TEM image. The red line in a) is the best fit of the histogram to a log-normal distribution with centre ± standard deviation σ of *D*=31±8 nm ($r^2$=0.987).

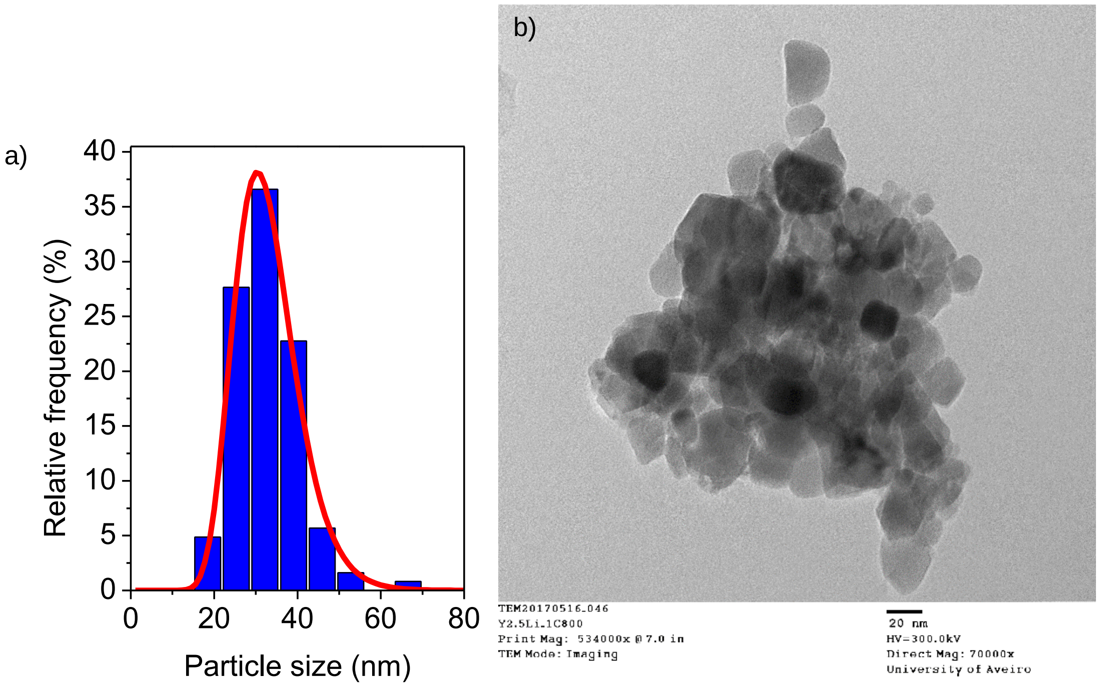

Figure 22: a) Histogram of the particle size distribution for 1.1 mol% $Li^+$ in $Y_2O_3$: Yb/Er (2/1 mol%) nanoparticles; b) TEM image. The red line in a) is the best fit of the histogram to a log-normal distribution with centre ± standard deviation σ of $D$=32±7 nm ($r^2$=0.991).

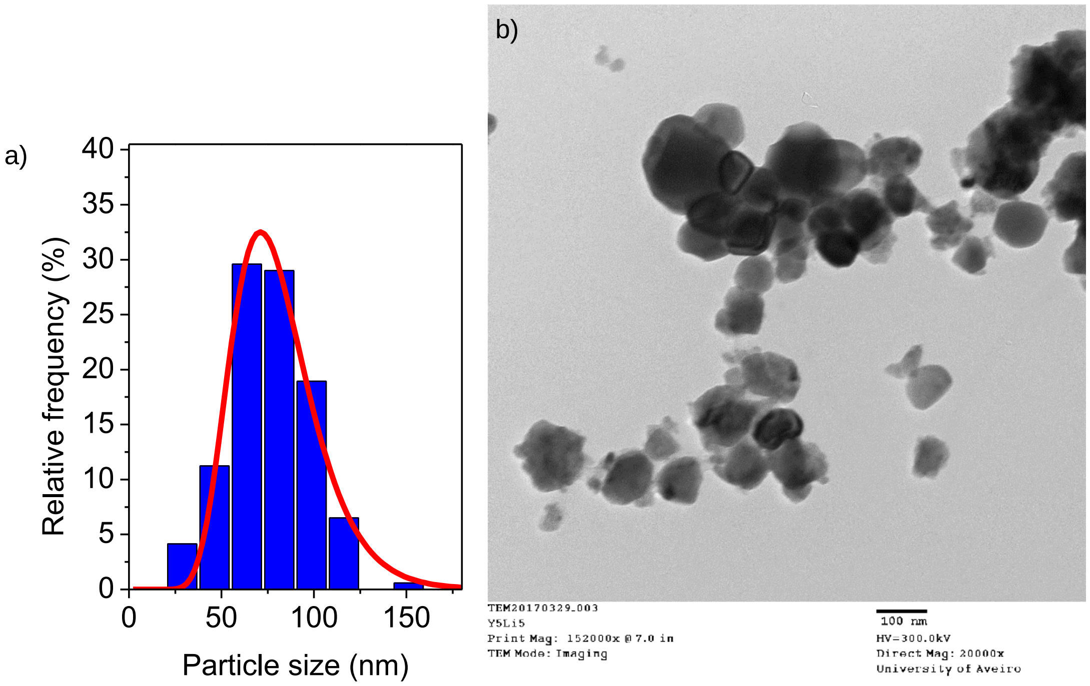

Figure 23: a) Histogram of the particle size distribution for 4.8 mol% $Li^+$ in $Y_2O_3$: Yb/Er (2/1 mol%) nanoparticles; b) TEM image. The red line in a) is the best fit of the histogram to a log-normal distribution with centre ± standard deviation σ of $D$=77±22 nm ($r^2$=0.959).

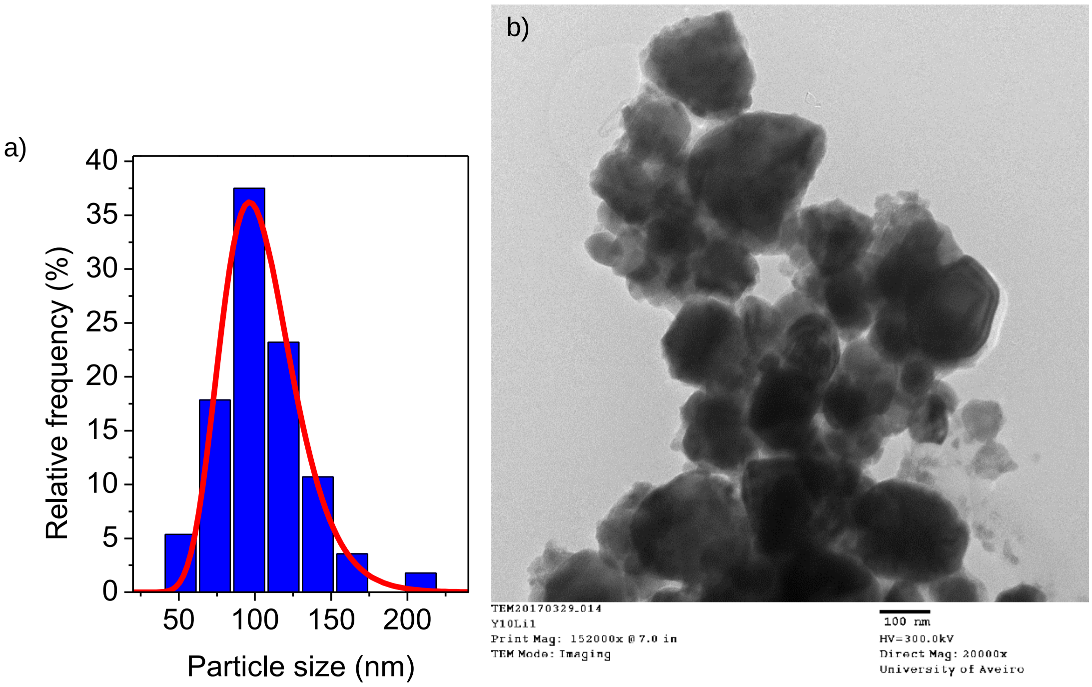

Figure 24: a) Histogram of the particle size distribution for 12.3 mol% $Li^+$ in $Y_2O_3$: Yb/Er (2/1 mol%) nanoparticles; b) TEM image. The red line in a) is the best fit of the histogram to a log-normal distribution with centre ± standard deviation σ of $D$=102±24 nm ($r^2$=0.967).

The nanoparticle sizes are collected in Table 4 and depicted in Figure 25. An increase of particle size with increasing $Li^+$ concentration is observed.

Table 4: Particle sizes of $Y_2O_3$: $Yb^{3+}/Er^{3+}$ (2/1 mol%) nanoparticles with 0, 0.8, 1.1, 4.8 and 12.3 mol% $Li^+$ obtained by TEM.

| **Li-composition** (mol%) | **Particle size** (nm) |
|---|---|
| 0 | 21 ± 5 |
| 0.8 | 31 ± 8 |
| 1.1 | 32 ± 7 |
| 4.8 | 77 ± 22 |
| 12.3 | 102 ± 24 |

The particle sizes obtained by XRD and TEM are plotted together in Figure 25 and are in good agreement. A particle and/or crystallite size increase with increasing $Li^+$ doping concentration is also observed for other upconversion nanoparticles with $GdVO_4$ [64] (phosphor with particle sizes in range of µm) $Lu_2O_3$ [34], $Lu_6O_5F_8$ [88], $Y_2SiO_3$[47, 53, 111], and $Y_2O_3$ [46, 47, 51] as host materials. Particle size increase may be due to a flux effect for the reaction by $Li^+$ ions as $LiNO_3$ melts above 255 °C. [88] Chen *et al.*, investigated the flux effect of $Li_2CO_3$ leading to higher crystallinity and larger crystallites [112]. As a reason, they propose the lower melting temperature of $Li_2CO_3$ whereby it melts first and generates a liquid phase at high temperature calcination. The liquid phase facilitates diffusion of ions and therefore accelerates the crystallization process. [113] In addition, crystallite growth is promoted by the formation of a liquid phase between the grain boundaries, which decreases energy loss on the surface. [114] This is one of the reasons why the particles agglomerate. The particles could be coated or surfactants could be used to separate the nanoparticles and to prevent agglomeration.

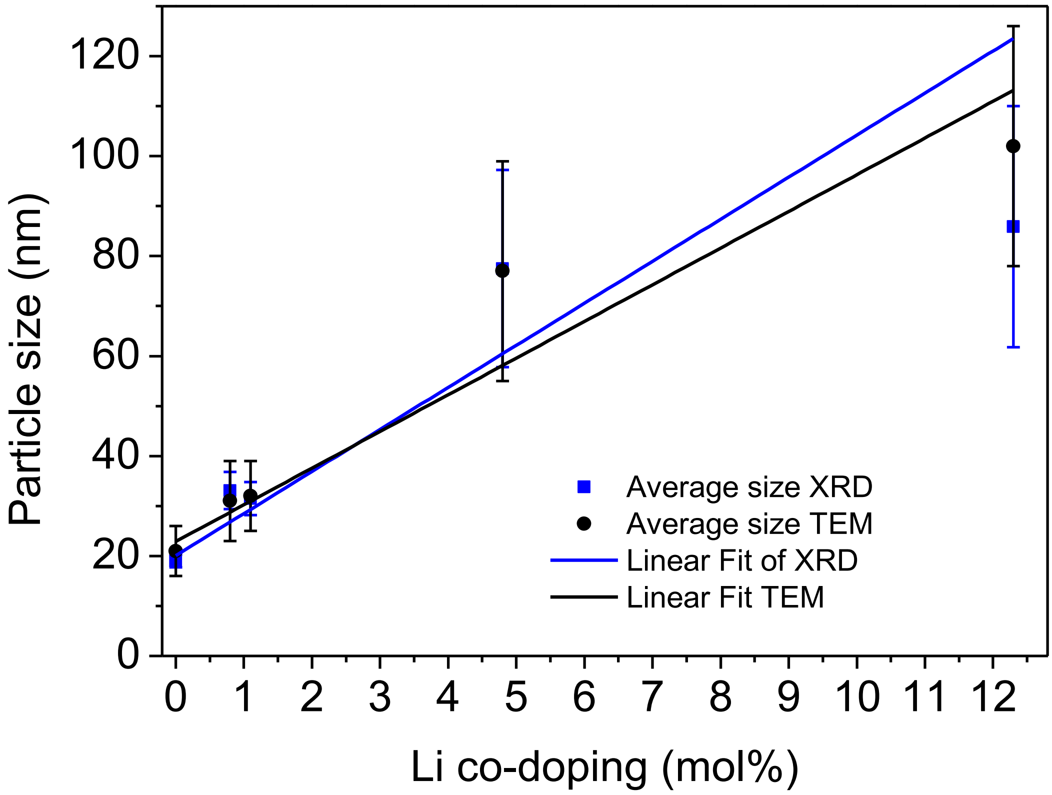

Figure 25: Evolution of particle size with Li doping obtained by XRD and TEM

### 4.2.4 Fourier Transform Infrared Spectroscopy

Figure 26 depicts FTIR transmittance spectra of $Y_2O_3$: $Yb^{3+}/Er^{3+}$ (2/1 mol%) nanoparticles with 0, 4.8 and 12.3 mol% $Li^+$ doping. Absorption bands around 1500 $cm^{-1}$ are attributed to carbonate groups $CO_2^{3-}$ due to adsorption of $CO_2$ on the surface of the nanoparticles. [101] The presence of $OH^-$ species adsorbed on the nanocrystalline surface have vibrational energies of 3350 $cm^{-1}$. [101] It is often stated that $Li^+$ ions decrease the amount of quenching centres ($OH^-$, $CO_2^{3-}$, etc.) on the surface of the nanoparticles, increasing UC emission by decreasing non-radiative transitions. [16, 21, 31, 34, 39, 40, 43, 45-48, 52, 58] In contrast to this observation, it seems that for the $Y_2O_3$: $Yb^{3+}/Er^{3+}$ (2/1 mol%) nanoparticles with 0, 4.8 and 12.3 mol% $Li^+$ doping analysed in this thesis, the bands of $OH^-$ and $CO_3^{2-}$ increase with $Li^+$ doping. However, FTIR is neither a surface technique (when regarding nanoparticles) nor a quantitative technique and therefore conclusions on the amount of surface groups cannot be made.

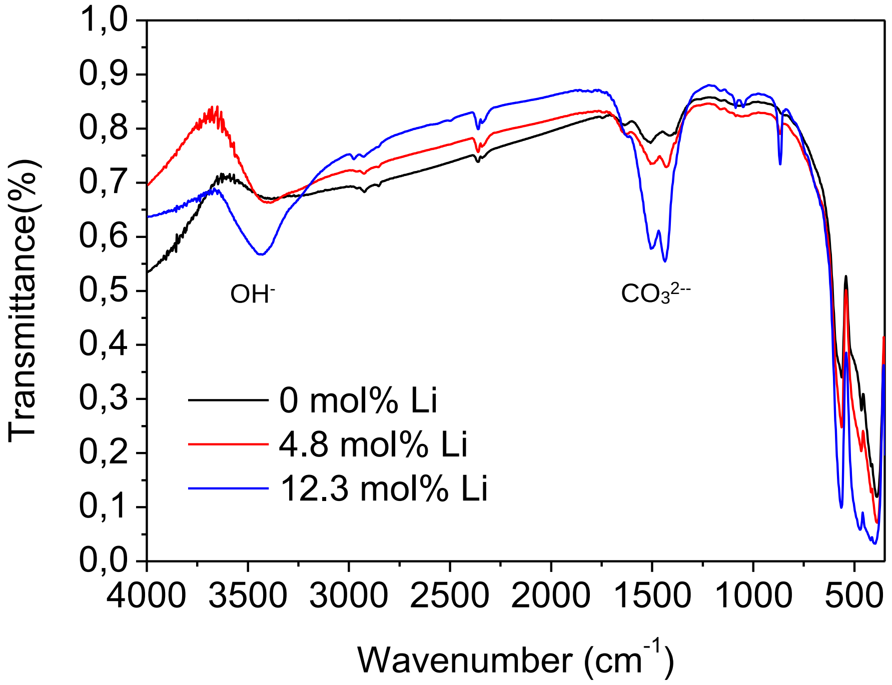

Figure 26: FTIR transmittance spectrum for $Y_2O_3$: $Yb^{3+}/Er^{3+}$ (2/1 mol%) nanoparticles with 0, 4.8 and 12.3 mol% $Li^+$.

### 4.2.5 Thermogravimetric Analysis

The weight loss and its derivative per Kelvin are plotted in Figure 27. The weight loss between room temperature and 800 °C for all samples is less than 1.5%: 1.49, 0.31, 0.28, 1.18, and 1.20% for 0, 0.8, 1.1, 4.8 and 12.3 mol%, respectively. The derivative weight per K has a minimum value of - 0.0014 % which corresponds to a maximum weight loss per K. Even the biggest weight loss is smaller than the half of the smallest observed values by Andelman *et al.,* for $Y_2O_3$ with different shapes. [115] The values are too small and the differences not significant enough to make a conclusion about the differences in the samples. Therefore no significant differences in the amount of hydroxyl and carbonate groups are observed for the samples.

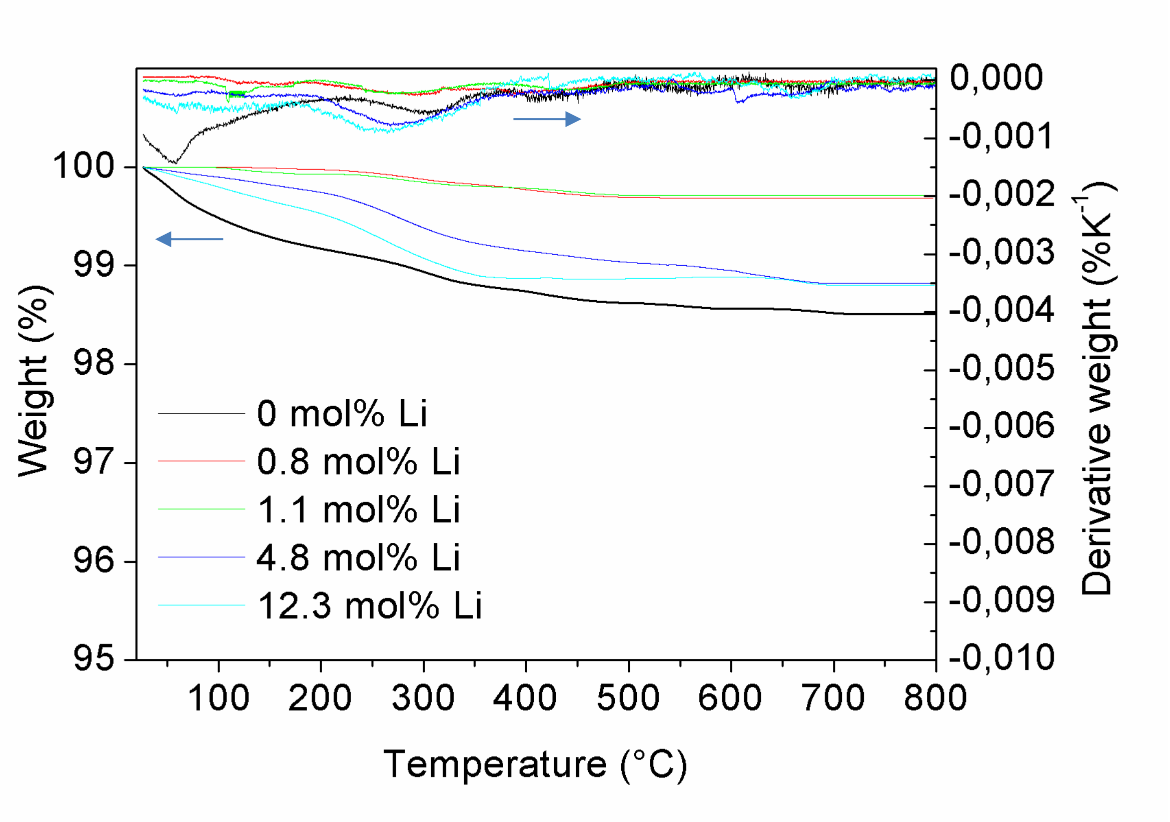

Figure 27: TGA of $Y_2O_3$: $Yb^{3+}/Er^{3+}$ (2/1 mol%) nanoparticles with 0, 0.8, 1.1, 4.8 and 12.3 mol% $Li^+$.

### 4.2.6 X-Ray Photoelectron Spectroscopy

Full XPS spectra of $Y_2O_3$: $Yb^{3+}/Er^{3+}$ (2/1 mol%) nanoparticles with 1.1 and 12.3 mol% $Li^+$ content are depicted in Figure 28, and a zoom of a selected region in Figure 29. At around 980 eV, the O Auger peak can be observed for both samples. At around 530 and 290 nm the peaks of O1s and C1s, respectively, are observed. For Y, more peaks are visible the Y3s, Y3p, Y3d, Y4s and Y4p are observed at around 390 eV, 300, 40 and 25 eV, respectively. The carbon C1s peak for nanoparticles with 1.1 mol% $Li^+$ content is higher than for samples doped with 12.3 mol% which means that more carbon based groups are present on the surface of the nanoparticles. As nanoparticles doped with 1.1 mol% are smaller than the 12.3 mol% particles (32±7 nm compared to 102±24 nm) their surface-to-volume ratio is higher and more $CO_2$ can be adsorbed on the surface of the nanoparticles. A quantitative analysis of the spectra and a XPS spectra for nanoparticles without $Li^+$ doping would be needed to confirm the trend of increasing carbon surface groups with increasing $Li^+$ concentration.

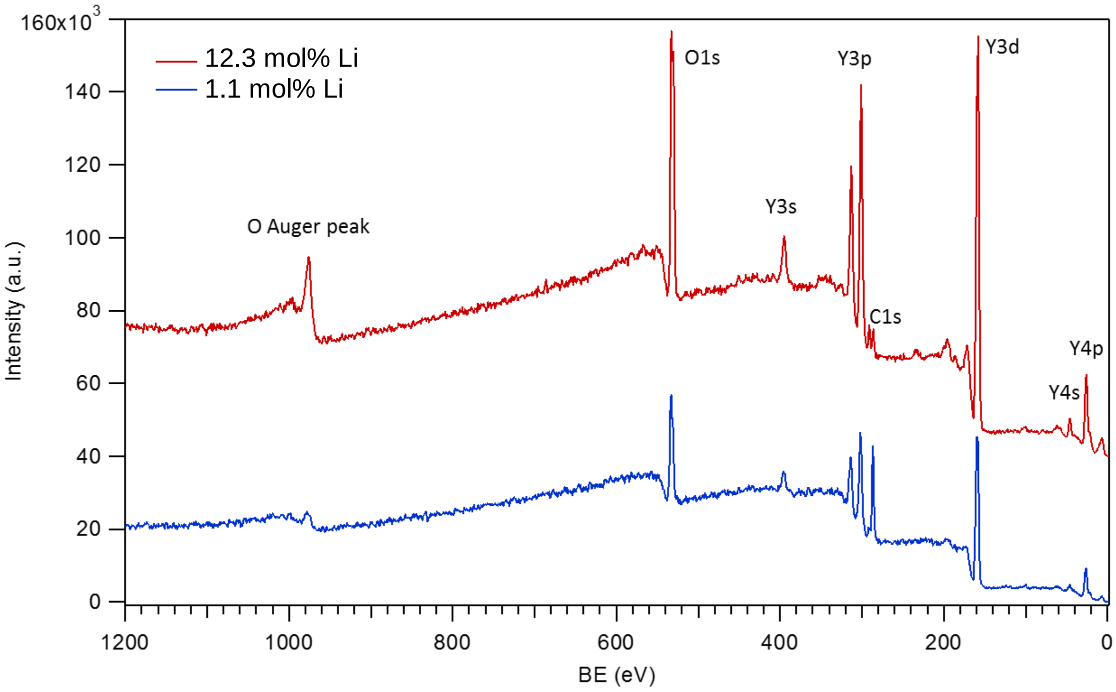

Figure 28: XPS spectra of 1.1 and 12.3 mol% $Li^+$ doped $Y_2O_3$: $Yb^{3+}/Er^{3+}$ (2/1 mol%) nanoparticles.

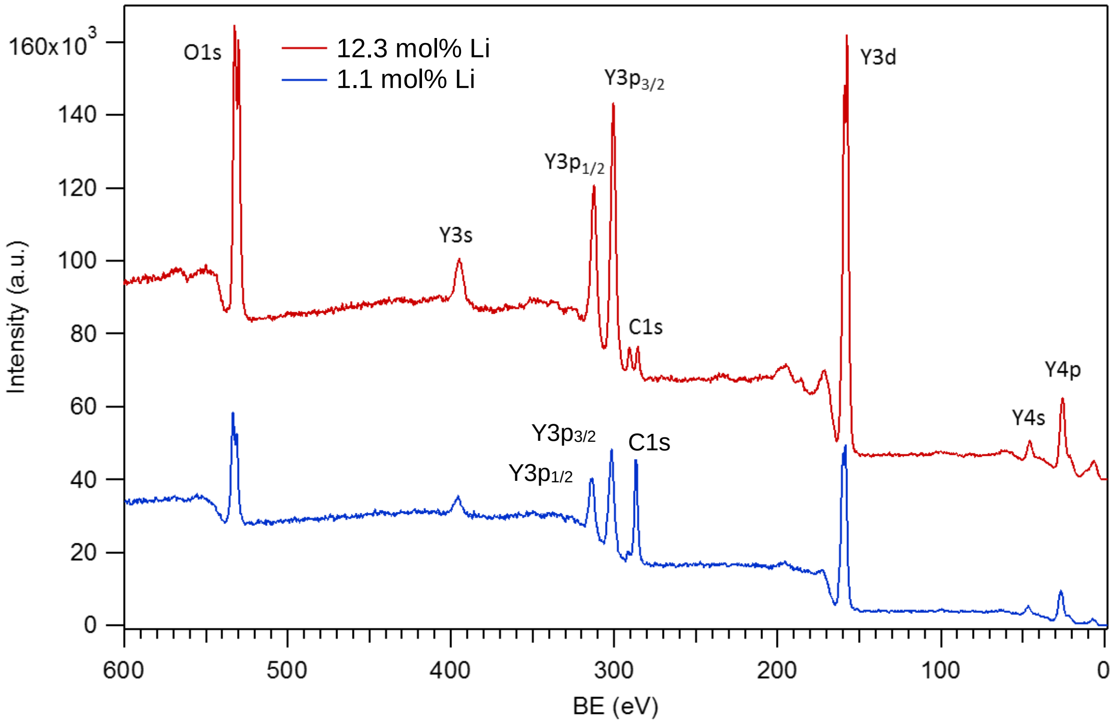

Figure 29: Selected region of the XPS spectra for 1.1 and 12.3 mol% $Li^+$ doped $Y_2O_3$: $Yb^{3+}/Er^{3+}$ (2/1 mol%) nanoparticles.

The main intensity of the C1s XPS peak identified as adventitious carbon, a thin layer of carbonaceous material on the surface of most air exposed samples, is used to charge reference the spectra of non-conducting specimen even if the signal differs slightly in diverse compounds. [116, 117] Therefor the spectra needs to be corrected by the difference between the measured C1s signal and its reference at 284.6 eV, proposed by Boyd *et al.,* [118] Consequently, all spectra for 1.1 mol% $Li^+$ content need to be corrected by (284.6 eV - 286.8 eV) -2.2 eV and for the 12.3 mol% $Li^+$ samples by (284.6 eV - 285.6 eV) -1.0 eV. The carbon C1s signals at (290.8-1.0 eV->) 289.8 eV and (291.3-2.2 eV->) 289.1 eV for 12.3 and 1.1 mol% $Li^+$, respectively, can be attributed to a C-O bond proposed by Bhattacharyya *et al.,* at 289.6 eV. [119]

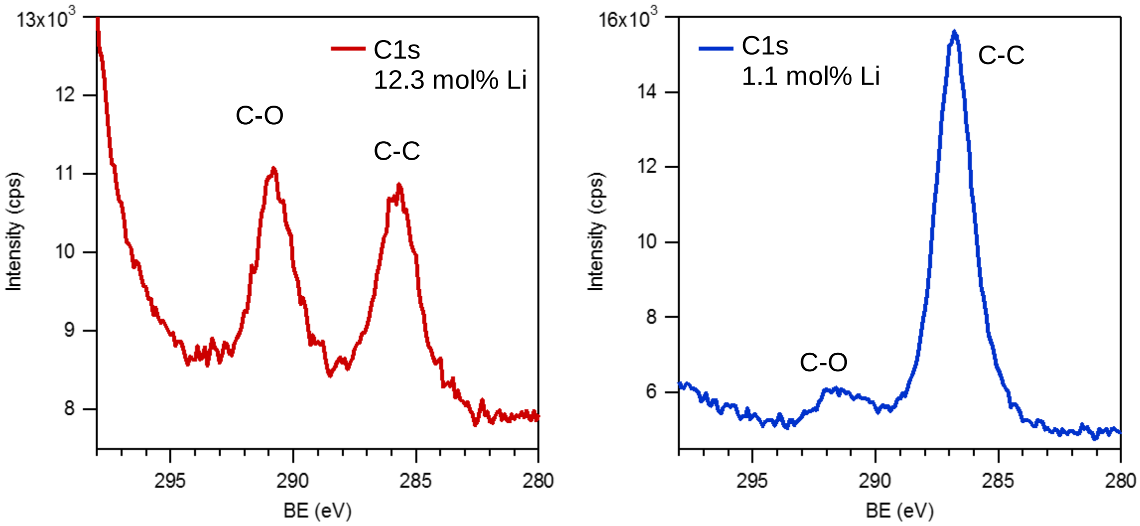

Figure 30: Carbon C1s peaks for a) 12.3 and b) 1.1 mol% $Li^+$ doped $Y_2O_3$: $Yb^{3+}/Er^{3+}$ (2/1 mol%) nanoparticles.

The O1s peaks positioned at (531.2-2.2 eV->) 529.0 eV and (530.1 eV-1 eV->) 529.1 eV for 1.1 and 12.3 mol% $Li^+$ content, respectively are attributed to $Y_2O_3$ by Majumdar *et al.,* (528.8 eV) [120] and Vasquez *et al.,* (528.9 eV) [121], respectively. The O1s peaks positioned at (533.5 eV-2.2 eV->) 531.3eV and (532.5-1.0 eV->) 531.5 eV for 1.1 and 12.3 mol% $Li^+$ content, respectively can be attributed to OH groups. Taking the relative heights of all peaks into account, no significate change of the amount of oxygen groups can be observed.

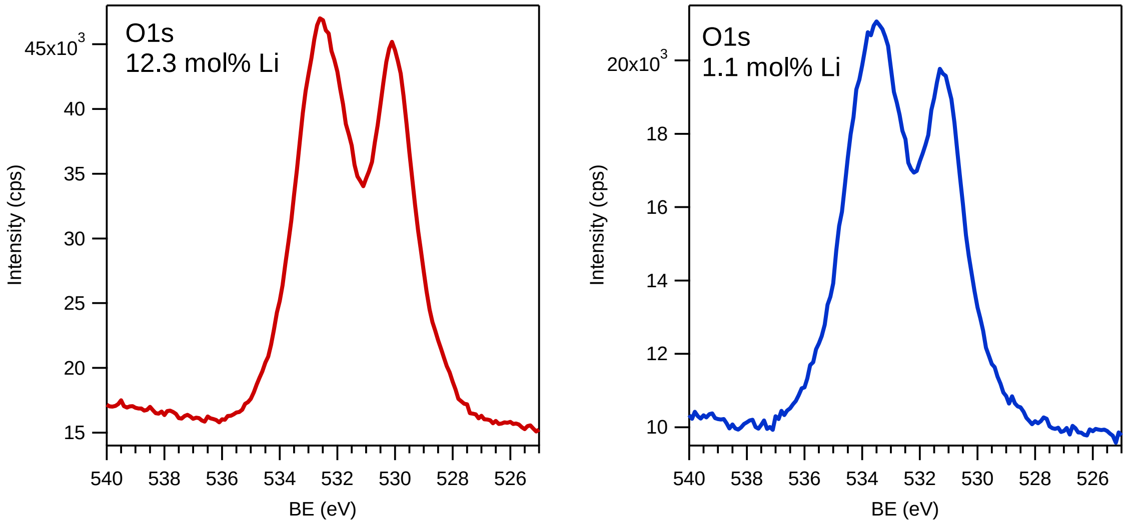

Figure 31: Oxygen O1s peak for a) 12.3 and b) 1.1 mol% Li$^+$ doped $Y_2O_3$: $Yb^{3+}/Er^{3+}$ (2/1 mol%) nanoparticles.

Figure 32 depicts XPS spectra for samples with a) 12.3 and b) 1.1 mol% Li content. A signal for the Li1s at (56.9 eV-1.0 eV->) 55.9 eV proves Li on the surface of the 12.3 mol% doped nanoparticles. For 1.1 Li no clear signal for the Li1s can be observed. However, a deconvolution could lead to a signal as ICP proved the Li incorporation.

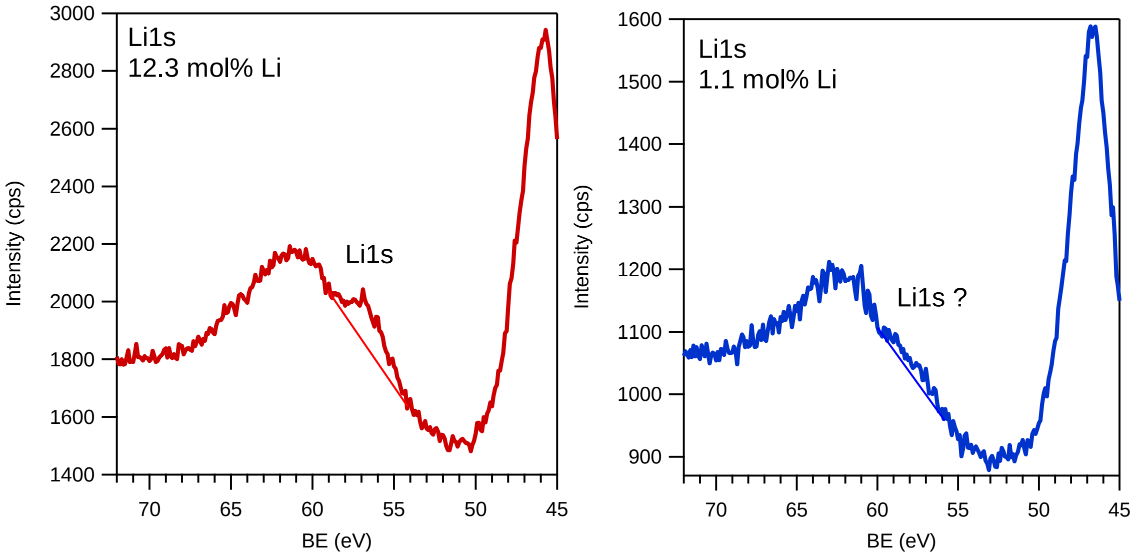

Figure 32: Lithium Li1s peaks for a) 12.3 and b) 1.1 mol% Li$^+$ ions doping of $Y_2O_3$: $Yb^{3+}/Er^{3+}$ (2/1 mol%) nanoparticles.

The signals of Er and Yb overlap with the Y signals and, as the amount of the latter is a magnitude higher, the signals are very small or not visible in the Y3d energy loss. Only the

Yb 4d signal can be observed at (185.8 eV-1.0 eV->) 184.8 eV for 12.3 mol% Li and at (186.8 eV-2.2 eV->184.6 eV) for 1.1 mol% Li content.

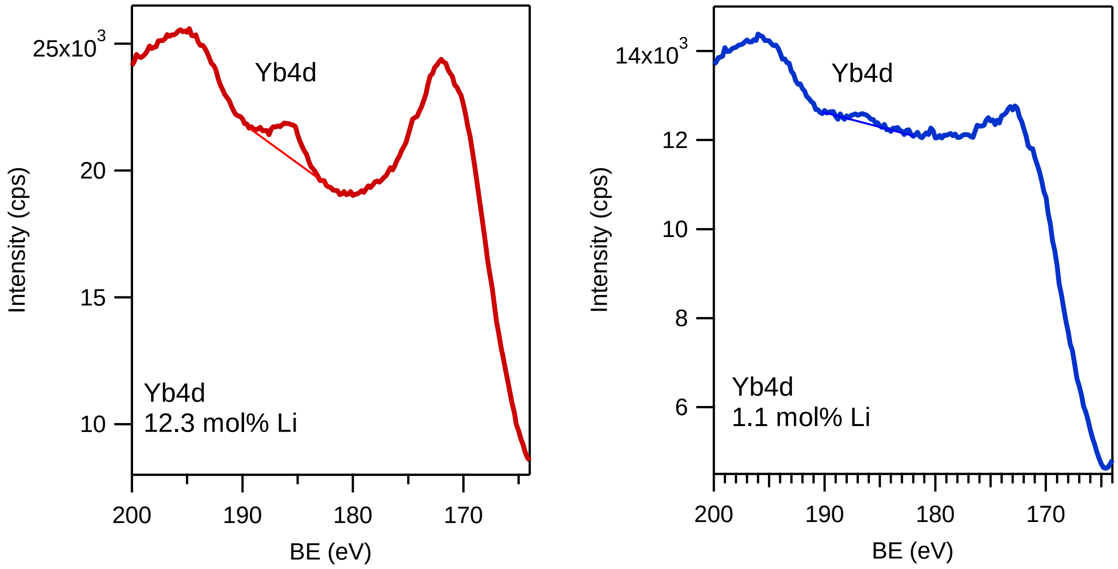

Figure 33: Yb4d peak in spectra measured with a higher pass-energy of 35 eV.

As a conclusion XPS proved the Li incorporation in the surface of the sample, carbon groups on the surface decrease with increasing Li doping and no change of the amount of OH groups is observed. Deconvolution is needed for quantitative analysis. High carbon contamination could be decreased by argon cleaning.

### 4.2.7 Radiant Flux Measurements Using an Integrating Sphere

In order to quantify the effect of $Li^+$ ion doping on up-conversion emission of $Y_2O_3$: $Yb^{3+}/Er^{3+}$ (2/1 mol%) nanoparticles radiant flux measurements are analysed. In contrast to analysing the intensity of up-conversion emission, which is given in arbitrary units (a.u.), the radiant flux is a quantitative measure of the UC emission and therefore enables the comparison of different samples. As an example for the up-conversion emission Figure 34 shows a photograph of a 1.1 mol% $Li^+$ doped sample irradiated with a 980 nm laser source with a laser power density of 400 $W/cm^2$. Green and red emission is observed. A detailed analysis of the effect of $Li^+$ ion doping on $Y_2O_3$: $Yb^{3+}/Er^{3+}$ (2/1 mol%) nanoparticles up-conversion is analysed in this chapter.

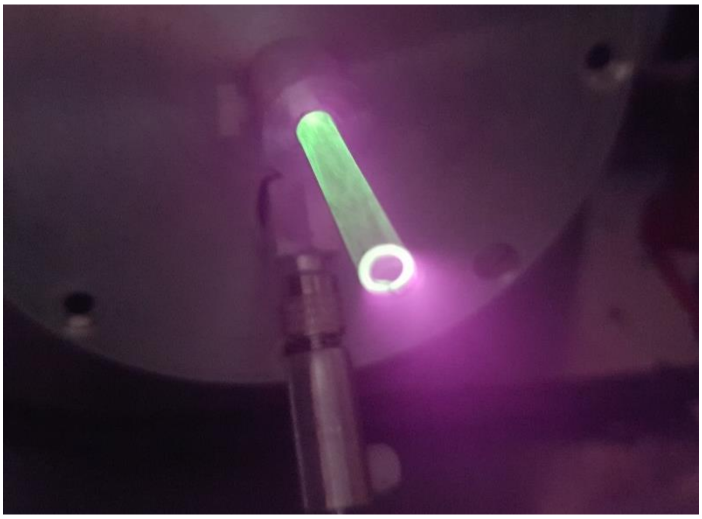

Figure 34: Photograph of $Y_2O_3$: $Yb^{3+}/Er^{3+}$ nanoparticles doped with 1.1 mol% $Li^+$ ions irradiated with a 980 nm laser source with a laser power density of 400 W/cm$^2$.

Figure 35 depicts the emission spectral flux for $Y_2O_3$: $Yb^{3+}/Er^{3+}$ nanoparticles doped with 0-12.3 mol% Li excited with a 980 nm laser source and a laser power density of 179 Wcm$^{-2}$. From the spectral flux several information can be taken. First both the green and red up-conversion emission are enhanced by $Li^+$ doping. Small amounts of $Li^+$ doping (0.8 and 1.1 mol%) enhance the green emission more efficient whereas bigger amounts (4.8 and 12.3 mol%) enhance more the red UC emission. The effect of the green/red ratio will be analysed more in detail at the end of this chapter. Another information is the overall enhancement of the up-conversion emission. To quantify this the up-conversion quantum yield is discussed in the following.

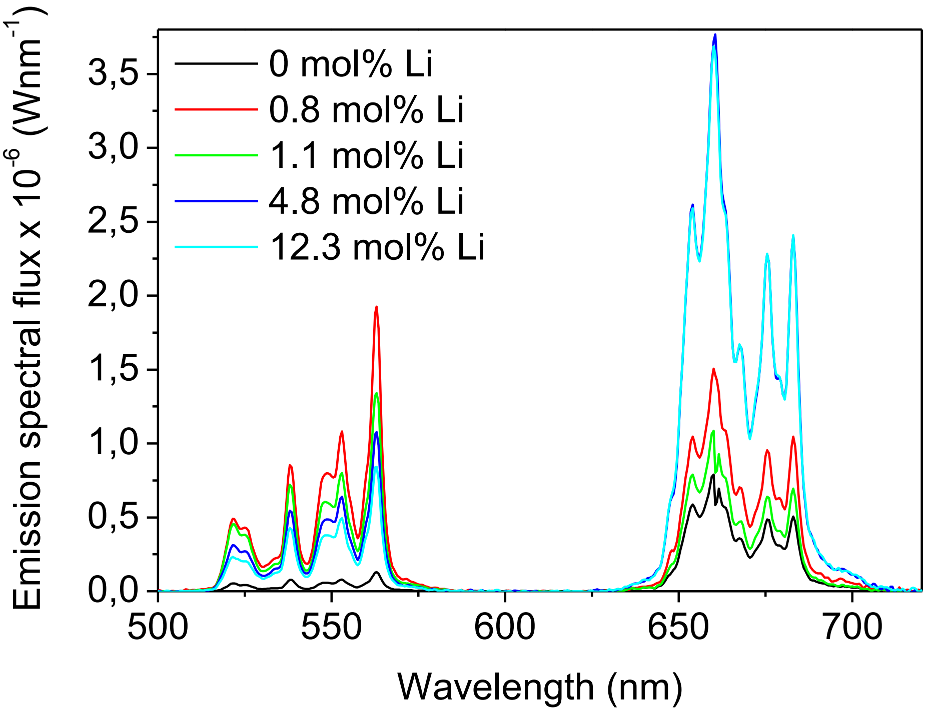

Figure 35: Emission spectral flux comparison for $Y_2O_3$: $Yb^{3+}/Er^{3+}$ nanoparticles doped with 0-12.3 mol% Li excited with a 980 nm laser source and a laser power density of 179 Wcm$^{-2}$.

To obtain the values for the UC quantum yields the radiant flux is analysed for laser power densities between 40 and 530 W/cm$^2$ and Figure 36 proves a linear increase with increasing laser power density for all samples. Li-undoped samples possess the smallest values followed by 0.8 and 1.1 mol% $Li^+$ doped samples and the highest values are observed for 4.8 and 12.3 mol% $Li^+$ doping.

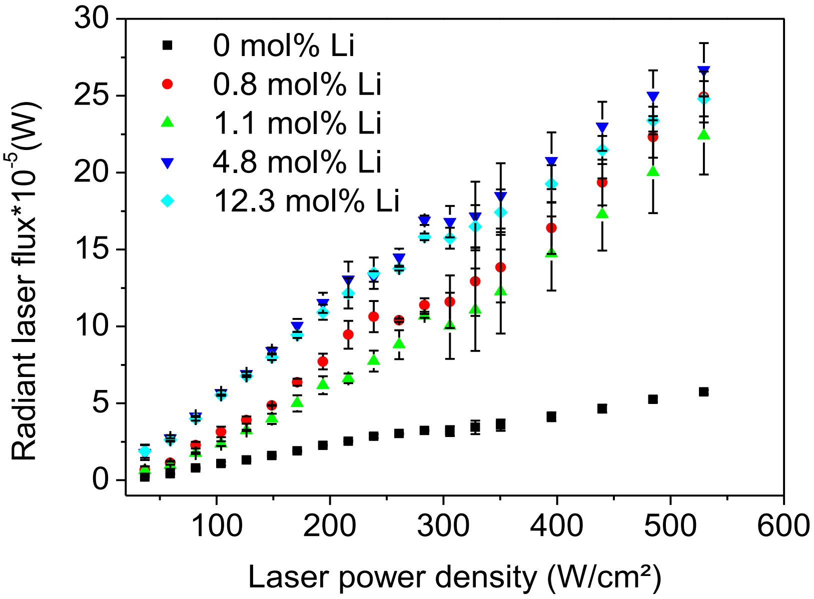

Figure 36: Dependence of radiant flux on the concentration of Li for $Y_2O_3$:$Yb^{3+}$/$Er^{3+}$ (2/1 mol%) nanoparticles doped with 0, 0.8, 1.1, 4.8 and 12.3 mol% $Li^+$.

Taking the radiant flux values the quantum yield values are calculated with equation (11) and depicted in Figure 37for $Y_2O_3$: $Yb^{3+}$/$Er^{3+}$ (2/1 mol%) nanoparticles with Li concentrations of 0, 0.8, 1.1, 4.8 and 12.3 mol%. The corresponding errors are obtained by combination of statistical and experimental errors, calculated by equation (12). In the low excitation power density regime the quantum yield values increase linearly until they reach a maximum/saturation value at 105 ± 25 $Wcm^{-2}$ for 0, 4.8 and 12.3 mol% $Li^+$ ion doping concentration and at 240 ± 30 $Wcm^{-2}$ for 0.8 and 1.1 mol% Li content. The maximum value of the emission quantum yield determines the onset of the saturation regime as discussed in the literature for $NaYF_4$:$Yb^{3+}$/$Er^{3+}$ [103,90] and $SrF_2$:$Yb^{3+}$/$Er^{3+}$ up-converting nanoparticles [103, 105] as well as for $NaYF_4$:$Yb^{3+}$/$Er^{3+}$ [122, 123] and $La_2S_3$:$Yb^{3+}$/$Er^{3+}$ bulk phosphors. [124] With a value of 0.0040 ± 0.0012 % the quantum yield for Li-undoped $Y_2O_3$: $Yb^{3+}$/$Er^{3+}$ (2/1 mol%) nanoparticles with a diameter of 21 ± 5 nm at the onset of the saturation regime (105 ± 25 $Wcm^{-2}$) is below the value measured for $SrF_2$:$Yb^{3+}$/$Er^{3+}$ (20/2%) up-converting nanoparticles (average size ~40 nm) at 390 ± 30 $Wcm^{-2}$ of 0.0057 ± 0.0006 % [103, 105], both measured for powders. However, the $Li^+$ content can increases the quantum yield up to ~5 times for 4.8 and 12.3 mol% $Li^+$ doping concentrations. This means that these nanoparticles possess quantum yields ~3.5 times higher than the maximum quantum yield reported for $SrF_2$:$Yb^{3+}$/$Er^{3+}$ up-converting nanoparticles.[103] The quantum yield values for 0.8 and 1.1 mol% Li (both with an average size of around 30 nm) are 0.0148 ± 0.0049 % and 0.0125 ± 0.0031 %, respectively (at 240 ± 30 $Wcm^{-2}$). The quantum yield values for 4.8 and 12.3 mol% Li (average size ~80 nm, and ~100 nm, respectively) are 0.0200 ± 0.0049 % and 0.0187 ± 0.0031 %, respectively (at 105 ± 25 $Wcm^{-2}$). As discussed in chapter 1 there is a debate about the reason of the up-conversion enhancement in literature. The most common mentioned reasons for up-conversion enhancement are a tailoring of the local surrounding around the activator and the reduction of quenching centres (like OH, $CO_3^{2-}$, etc.). FTIR and XPS data prove the existence of OH groups in the sample but no significant changes with increasing Li content between 0-12.3 mol% Li are observed which is often used as an explanation for up-conversion enhancement. [16, 21, 31, 34, 39, 40, 43, 45-48, 52, 58] Moreover, thermogravimetric analysis for $Y_2O_3$: $Yb^{3+}/Er^{3+}$ (2/1 mol%) nanoparticles shows no significant weight change up to 800 °C, which excludes again the explanation by the decrease of OH-groups. Also a size increase as sometimes taken as an explanation for the up-conversion enhancement. [20, 34, 46, 47] However, it cannot be a crucial factor for the enhancement as Li-undoped nanoparticles synthesized by sol–gel mixing and solid state reaction route possess diameters with a factor ~10 difference and no significant change in the quantum yield values is observed (Figure 37). However, XPS confirms the presence and decrease of carbon groups on the surface with increasing Li content for 1.1 to 12.3 mol%. As carbon groups on the surface act as quenching centres, they decrease the up-conversion emission by non-radiative transitions. A decrease of their amount therefore enhances the up-conversion emission. Rietveld refinement of powder XRD patterns cannot confirm a change of the unit cell parameter caused by the incorporation of $Li^+$ ions in the crystal lattice.

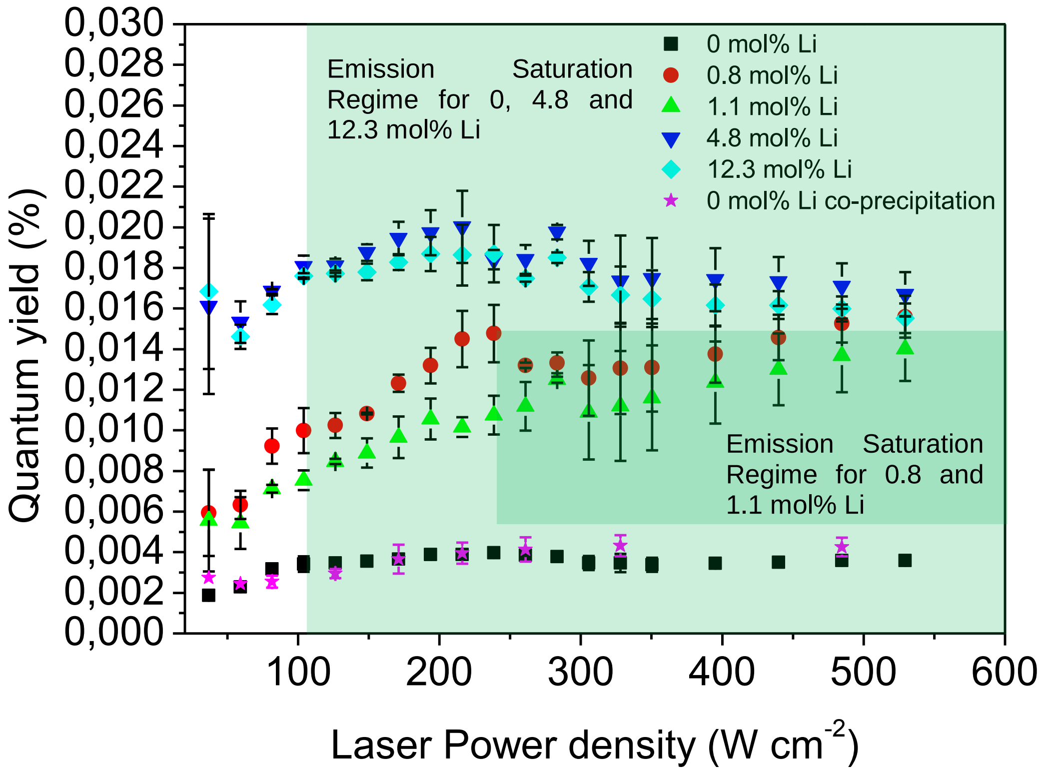

Figure 37: Dependence of quantum yield q on the concentration of $Li^+$ doping for $Y_2O_3$: $Yb^{3+}/Er^{3+}$ (2/1 mol%) nanoparticles.

The reproducibility of the quantum yield measurements for the same samples at the same irradiation spot are analysed for two cycles. The quantum yield values stay without significant change between the cycles whereby a reproducibility of the measurement and no burning effect of the powder can be assumed. The onset of the emission saturation regime is observed at 105±25 Wcm$^{-2}$ (and 240 ± 30 Wcm$^{-2}$ for 0.8 and 1.1 mol% Li content) where a linear increase changes into a plateau. A decrease of the quantum yield values in the saturation regime at higher laser power densities is observed and in accordance with the observation by Kaiser *et al.*. [125]

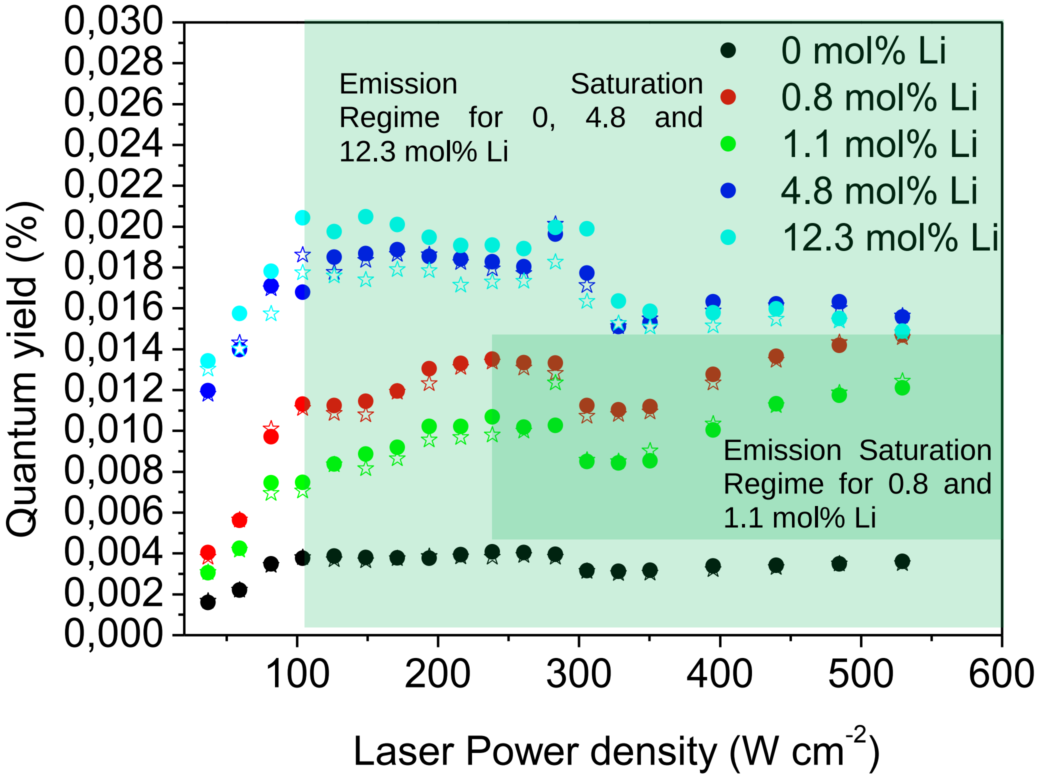

Figure 38: Cycling effect of measurements for dependence of quantum yield q on the concentration of Li doping.

The number of photons involved in the up-conversion process should be well characterized as it can give mechanistic insights in UC processes. [125] Therefore, the slope of the logarithm of UC luminescence intensity versus the logarithm of the laser power density, called log–log diagram, is depicted in Figure 39 for the green region between 500 and 600 nm and in Figure 40 for the red region between 620 and 720 nm. Photon up-conversion is a non-linear process which makes the emission quantum yield dependent on the excitation power density. [105, 122, 126] In the low excitation power density regime, the two-photon absorption process dominates the emission and therefore a slope equals to 2 characterizes the linear dependence of the integrated up-conversion intensity with the laser power density in a log-log plot. In the green region nanoparticles doped with 0, 0.8, 1.1, 4.8 and 12.3 mol% $Li^+$ follow this behaviour with values for the slope n of 2.1, 2.3, 2.0, 1.6 and 1.4, respectively. The size strongly influences the up-conversion process. [125] The smaller n values for 4.8 and 12.3 mol% $Li^+$ doped samples are explained by their bigger size compared to lower $Li^+$ doped samples. However, they give no precise explanation for it. For the red region the slope values are smaller than for the green region. As explained in chapter 2.7 the red emission is possible by several ways. A higher fraction of non-radiative transmissions leads to a decreased amount of photons which are effectively used for the UC process. Again nanoparticles doped with 0, 0.8 and 1.1 mol% with values for the slope of 1.8 follow this behaviour. Bigger nanoparticles doped with 4.8 and 12.3 mol% show smaller values for the slope of 1.4 and 1.3, respectively.

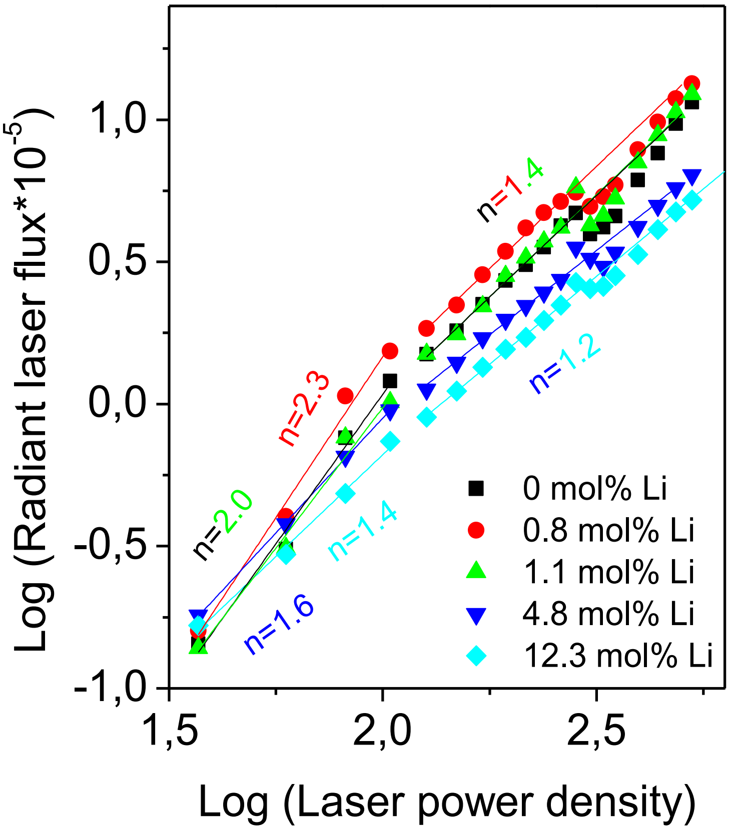

Figure 39: Log-log graph for $Y_2O_3$: $Yb^{3+}/Er^{3+}$ (2/1 mol%) nanoparticles doped with 0-12.3 mol% $Li^+$ obtained for the green region between 500 and 600 nm.

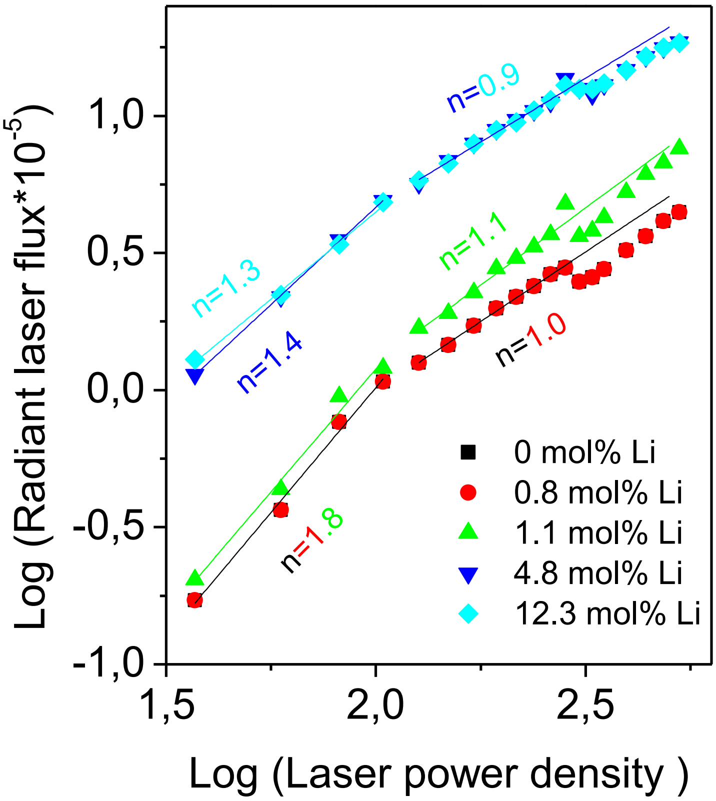

Figure 40: Log-log graph for $Y_2O_3$: $Yb^{3+}/Er^{3+}$ (2/1 mol%) nanoparticles doped with 0-12.3 mol% $Li^+$ obtained for the red region between 620 and 720 nm.

With increasing excitation power density, the competition between the up-conversion process and linear decays in the individual excitation steps starts to play an important role and this region is called emission saturation regime. [127-129] If the excitation intensity is high enough to induce such saturation of the intermediate energy state involved in the UC process, the multiphoton UC luminescence dependence on the laser power density presents a slope near 1. [76, 130] The slope for all nanoparticles is decreased beginning at 2.02±0.08 (which corresonds to a laser power density of 105±25 $Wcm^{-2}$) for the green region to 1.4 for 0, 0.8 and 1.1 mol% $Li^+$ ion content and 1.2 for nanoparticles doped with 4.8 and 12.3 mol% $Li^+$ ions. In the red region the slopes are 1.0 for 0 and 0.8 mol% Li content, 1.1 for 1.1 mol% $Li^+$ ions and 0.9 for 4.8 and 12.3 mol% $Li^+$ ion doping concentration.

Concluding, the decrease of n values of red and green emission with increasing laser power density is expected for saturation. [125] Moreover, n values of 2 in the low excitation power density regime and of 1 in the emission saturation regime are in accordance with the theory of up-conversion process. [76, 127-130]

As mentioned in the beginning of this chapter the green to red ratio is analysed more in detail in the following. Figure 41 depicts a spectral profile comparison of normalized intensities for $Y_2O_3$: $Yb^{3+}/Er^{3+}$ (2/1 mol%) nanoparticles doped with 0, 0.8, 1.1, 4.8 and 12.3 mol% $Li^+$ ions at a laser power density of 171 $W/cm^{-2}$ in a) and their integrated green to red ratios in b). Starting from Li-undoped nanoparticles with a value of 0.13, the green to red ratio of integrated normalized spectra increases to 0.68 and further to 0.97 for 0.8 and 1.1 mol% $Li^+$ ion doping. This trend for low $Li^+$ doping concentrations is also observed by Jia *et al.,* [30] who attribute it to non-radiative multi-phonon relaxation processes in the activator which are weakened with increasing $Li^+$ doping concentration. However, with further increase of $Li^+$ doping concentration, the green to red ratio decreases to 0.21 and 0.17 for 4.8 and 12.3 mol% $Li^+$, respectively. The concentration of Er and Yb for samples doped with 4.8 and 12.3 mol% $Li^+$ ions are almost double as high as for lower $Li^+$ doping. Pires *et al.,* found a decrease of green to red ratio with increasing $Yb^{3+}$ independent of the host matrix or particle size and attributed it to an increased red transmission by increasing the energy transfer from $Yb^{3+}$ to $Er^{3+}$. [131] Singh *et al.,* also found an enhanced red emission for higher $Yb^{3+}$ concentrations in $ZrO_2$ but explained it by a cross-relaxation process between two nearby $Er^{3+}$ ions, $^4S_{3/2} + {}^4I_{15/2} \rightarrow {}^4I_{9/2} + {}^4I_{13/2}$. [132] Vetrone *et al.,* discovered the same phenomenon in nanocrystalline $Y_2O_3$:Yb/Er NCs and attributed it to the cross-relaxation of the $Er^{3+}$ states $^4F_{7/2} + {}^4I_{11/2} \rightarrow {}^4F_{9/2} + {}^4F_{9/2}$. [101] They also reported an enhancement in the red emission with elevating doping concentration of $Er^{3+}$. As both the $Er^{3+}$ and $Yb^{3+}$ concentration is higher for higher $Li^+$ doping these effects could play a role. In addition, if the doping of $Li^+$ decreases the distance between $Er^{3+}$ ions or between $Yb^{3+}$ and $Er^{3+}$ the red emission is enhanced. There are a lot of options but no proof can be given which effect is contributing to the changed red to green ratio. There is no correlation of the green/red ratio with the quantum yields.

a)

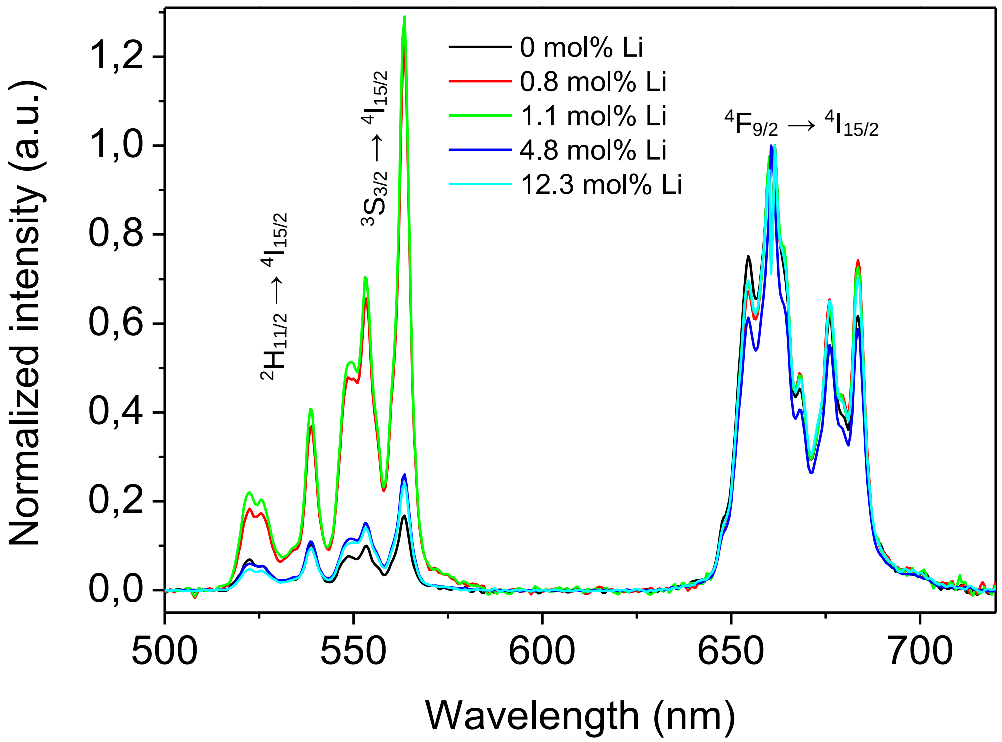

b)

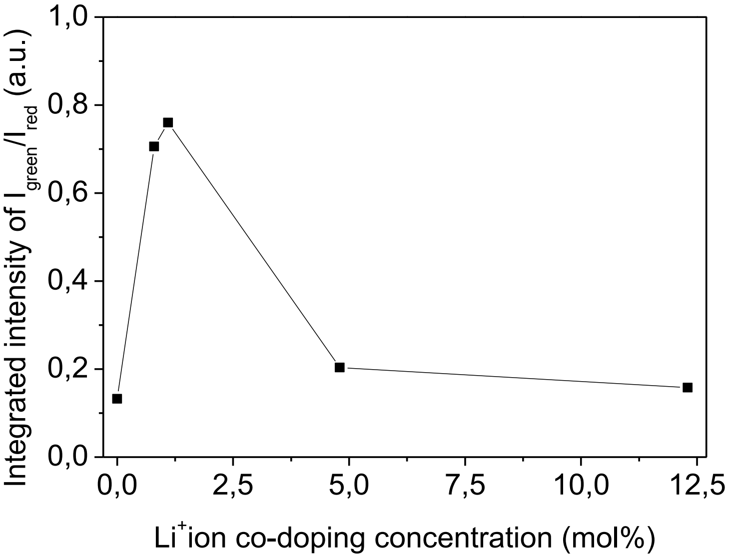

Figure 41: Comparison of normalized intensity spectra for $Y_2O_3$:$Yb^{3+}$/$Er^{3+}$ (2/1 mol%) nanoparticles with 0, 0.8, 1.1, 4.8 and 12.3 mol% $Li^+$ ions at 171 $W/cm^{-2}$ in a) and their integrated green/red ratio in b).

# 5 Conclusion

$Y_2O_3$: $Yb^{3+}/Er^{3+}$ (2/1 mol%) nanoparticles doped with $Li^+$ were synthesized by two different methods. In the first part of the project, the reflux/co-precipitation method used afforded round particles with tuneable sizes. However, ICP-AES analysis revealed that no $Li^+$ was incorporated in the nanoparticles. Therefore, another technique was used in the second part of the project. Even if a sol–gel mixing and solid-state reaction route has some drawbacks *e.g.,* the nanoparticles are not perfectly round, they agglomerate and the size control is more difficult, $Li^+$ incorporation was shown by ICP results. Therefore, the effect of $Li^+$ on the $Y_2O_3$: $Yb^{3+}/Er^{3+}$ (2/1 mol%) nanoparticle's up-conversion was studied. Starting from a value of $4 \pm 1 \times 10^{-3}$ %, the quantum yield of Li-undoped $Y_2O_3$: $Yb^{3+}/Er^{3+}$ (2/1 mol%) nanoparticles with a diameter of ~20 nm, $Li^+$ doping increased the quantum yield up to ~5 times for $Li^+$ concentrations of 4.8 and 12.3 mol%. The quantum yield values for 0.9 and 1.1 mol% Li (both with an average size ~30 nm) are ~3 times enhanced. FTIR and XPS data prove the presence of OH groups in the sample but no significant changes with increasing Li content between 0-12.3 mol% Li is observed which is often used as an explanation for up-conversion enhancement. Moreover, TGA analysis shows no significant weight change up to 800 °C, which excludes again the explanation of up-conversion by the decrease of the amount of OH-groups. Rietveld refinement of powder XRD patterns cannot confirm a change of the unit cell parameter caused by the incorporation of $Li^+$ ions in the crystal lattice. Also a size increase as an explanation of the up-conversion enhancement cannot be the main factor as nanoparticles without $Li^+$ ion content synthesized by a sol–gel mixing and solid state reaction route possess ~10 times smaller diameters than nanoparticles synthesized by a reflux/co-precipitation method and no significant change in the quantum yield values are observed. However, XPS confirms the presence and decrease of carbon groups on the surface with increasing Li content for 1.1 to 12.3 mol%. As carbon groups on the surface act as quenching centres, they decrease the up-conversion emission by non-radiative transitions. In addition to the enhancement of quantum yields by $Li^+$ ion doping the red/green ratio can be controlled. This is interesting as different applications use different wavelengths of the up-conversion emission. The red emission is important for bio-application due to a lower absorbance of tissue in the IR and red region. The green up-conversion emission is interesting in the field of temperature sensors. In the future the agglomeration needs to be controlled. Surface passivation could be a solution to get rid of quenching centres at the nanoparticle surfaces. Like this the effect of Li doping on the UC enhancement can be distinguished of surface effects.

# Literature

1. Z. Li and Y. Zhang, Nanotechnology **19** (34) (2008).
2. F. Wang, D. K. Chatterjee, Z. Li, Y. Zhang, X. Fan and M. Wang, Nanotechnology **17** (23), 5786-5791 (2006).
3. F. Sidiroglou, S. A. Wade, N. M. Dragomir, G. W. Baxter and S. F. Collins, Review of Scientific Instruments **74** (7), 3524-3530 (2003).
4. B. Dong, D. P. Liu, X. J. Wang, T. Yang, S. M. Miao and C. R. Li, Applied Physics Letters **90** (18) (2007).
5. M. L. Debasu, C. D. S. Brites, S. Balabhadra, H. Oliveira, J. Rocha and L. D. Carlos, Chemnanomat **2** (6), 520-527 (2016).
6. S. Balabhadra, M. L. Debasu, C. D. S. Brites, L. A. O. Nunes, O. L. Malta, J. Rocha, M. Bettinelli and L. D. Carlos, Nanoscale **7** (41), 17261-17267 (2015).
7. M. L. Debasu, D. Ananias, I. Pastoriza-Santos, L. M. Liz-Marzan, J. Rocha and L. D. Carlos, Advanced Materials **25** (35), 4868-4874 (2013).
8. X. Y. Huang, S. Y. Han, W. Huang and X. G. Liu, Chemical Society Reviews **42** (1), 173-201 (2013).
9. M. L. Debasu, D. Ananias, S. L. C. Pinho, C. Geraldes, L. D. Carlos and J. Rocha, Nanoscale **4** (16), 5154-5162 (2012).
10. S. Y. Han, R. R. Deng, X. J. Xie and X. G. Liu, Angewandte Chemie-International Edition **53** (44), 11702-11715 (2014).
11. Y. Bai, Y. Wang, K. Yang, X. Zhang, Y. Song and C. H. Wang, Optics Communications **281** (21), 5448-5452 (2008).
12. Y. Bai, K. Yang, Y. Wang, X. Zhang and Y. Song, Optics Communications **281** (10), 2930-2932 (2008).
13. G. Y. Chen, H. C. Liu, G. Somesfalean, Y. Q. Sheng, H. J. Liang, Z. G. Zhang, Q. Sun and F. P. Wang, Applied Physics Letters **92** (11) (2008).
14. C. Mao, X. Yang and L. Zhao, Chemical Engineering Journal **229**, 429-435 (2013).
15. X. Zhang, M. Wang, J. Ding, D. Gao, Y. Shi and X. Song, Crystengcomm **14** (24), 8357-8360 (2012).
16. A. Dubey, A. K. Soni, A. Kumari, R. Dey and V. K. Rai, Journal of Alloys and Compounds **693**, 194-200 (2017).
17. Y. L. Ding, X. D. Zhang, H. B. Gao, S. Z. Xu, C. C. Wei and Y. Zhao, Journal of Alloys and Compounds **599**, 60-64 (2014).
18. Q. Q. Dou and Y. Zhang, Langmuir **27** (21), 13236-13241 (2011).
19. H. Lin, D. K. Xu, D. D. Teng, S. H. Yang and Y. L. Zhang, Optical Materials **45**, 229-234 (2015).
20. M. Misiak, B. Cichy, A. Bednarkiewicz and W. Strek, Journal of Luminescence **145**, 956-962 (2014).
21. Q. Sun, X. Q. Chen, Z. K. Liu, F. P. Wang, Z. H. Jiang and C. Wang, Journal of Alloys and Compounds **509** (17), 5336-5340 (2011).
22. X. Q. Chen, Z. K. Liu, Q. Sun, M. Ye and F. P. Wang, Optics Communications **284** (7), 2046-2049 (2011).
23. Y. K. Cun, Z. W. Yang, J. Y. Liao, J. B. Qiu, Z. G. Song and Y. Yang, Materials Letters **131**, 154-157 (2014).
24. T. Pang, W. H. Lu and W. J. Shen, Physica B-Condensed Matter **502**, 11-15 (2016).
25. Y. Y. Guo, D. Y. Wang and F. Wang, Optical Materials **42**, 390-393 (2015).
26. P. Singh, P. K. Shahi, A. Rai, A. Bahadur and S. B. Rai, Optical Materials **58**, 432-438 (2016).
27. A. P. Jadhav, J. H. Oh, S. W. Park, H. Choi, B. K. Moon, B. C. Choi, K. Jang, J. H. Jeong, S. S. Yi and J. H. Kim, Current Applied Physics **16** (10), 1374-1381 (2016).

28. D. G. Li, W. P. Qin, P. Zhang, L. L. Wang, M. Lan and P. B. Shi, Optical Materials Express **7** (2), 329-340 (2017).
29. H. H. T. Vu, T. S. Atabaev, N. D. Nguyen, Y. H. Hwang and H. K. Kim, Journal of Sol-Gel Science and Technology **71** (3), 391-395 (2014).
30. Y. T. Jia, Y. L. Song, Y. F. Bai and Y. X. Wang, Luminescence **26** (4), 259-263 (2011).
31. Q. Sun, H. Zhao, X. Q. Chen, F. P. Wang, W. Cai and Z. H. Jiang, Materials Chemistry and Physics **123** (2-3), 806-810 (2010).
32. J. Y. Sun, B. Xue and H. Y. Du, Infrared Physics & Technology **60**, 10-14 (2013).
33. J. Y. Sun, B. Xue and H. Y. Du, Optics Communications **298**, 37-40 (2013).
34. L. Li, X. T. Wei, X. Q. Cao, K. M. Deng, Q. H. Chen, Y. H. Chen, C. X. Guo and M. Yin, Journal of Nanoscience and Nanotechnology **11** (11), 9892-9898 (2011).
35. B. S. Cao, Y. Y. He, Y. Sun, M. Song and B. Dong, Journal of Nanoscience and Nanotechnology **11** (11), 9899-9903 (2011).
36. B. S. Cao, Y. Y. He, Z. Q. Feng, M. Song and B. Dong, Optics Communications **284** (13), 3311-3314 (2011).
37. B. S. Cao, Z. Q. Feng, Y. Y. He, H. Li and B. Dong, Journal of Sol-Gel Science and Technology **54** (1), 101-104 (2010).
38. M. Z. Yang, Y. Sui, S. P. Wang, X. J. Wang, Y. Q. Sheng, Z. G. Zhang, T. Q. Lu and W. F. Liu, Chemical Physics Letters **492** (1-3), 40-43 (2010).
39. M. Z. Yang, Y. Sui, H. W. Mu, S. C. Lu, X. J. Wang and T. Q. Lu, Journal of Rare Earths **29** (11), 1022-1025 (2011).
40. Y. F. Bai, Y. X. Wang, G. Y. Peng, K. Yang, X. R. Zhang and Y. L. Song, Journal of Alloys and Compounds **478** (1-2), 676-678 (2009).
41. T. Fan and J. Lu, Optics Communications **300**, 5-7 (2013).
42. G. Y. Chen, H. C. Liu, H. J. Liang, G. Somesfalean and Z. G. Zhang, Solid State Communications **148** (3-4), 96-100 (2008).
43. Y. F. Bai, Y. X. Wang, G. Y. Peng, W. Zhang, Y. K. Wang, K. Yang, X. R. Zhang and Y. L. Song, Optics Communications **282** (9), 1922-1924 (2009).
44. Y. F. Bai, K. Yang, Y. X. Wang, X. R. Zhang and Y. L. Song, Optics Communications **281** (10), 2930-2932 (2008).
45. H. J. Liang, Y. D. Zheng, G. Y. Chen, L. Wu, Z. G. Zhang and W. W. Cao, Journal of Alloys and Compounds **509** (2), 409-413 (2011).
46. K. Mishra, S. K. Singh, A. K. Singh and S. B. Rai, Materials Research Bulletin **48** (10), 4307-4313 (2013).
47. R. V. Yadav, S. K. Singh and S. B. Rai, Rsc Advances **5** (33), 26321-26327 (2015).
48. A. Pandey, V. K. Rai and K. Kumar, Spectrochimica Acta Part a-Molecular and Biomolecular Spectroscopy **118**, 619-623 (2014).
49. H. J. Liang, G. Y. Chen, H. C. Liu and Z. G. Zhang, Journal of Luminescence **129** (3), 197-202 (2009).
50. E. F. Huerta, S. Carmona-Tellez, S. Gallardo-Hernandez, J. G. Cabanas-Moreno and C. Falcony, Ecs Journal of Solid State Science and Technology **5** (7), R129-R135 (2016).
51. G. Y. Chen, H. C. Liu, H. J. Liang, G. Somesfalean and Z. G. Zhang, Journal of Physical Chemistry C **112** (31), 12030-12036 (2008).
52. D. Y. Li, Y. X. Wang, X. R. Zhang, H. X. Dong, L. Liu, G. Shi and Y. L. Song, Journal of Applied Physics **112** (9), 5 (2012).
53. E. L. Cates, A. P. Wilkinson and J. H. Kim, Journal of Physical Chemistry C **116** (23), 12772-12778 (2012).
54. Z. S. Chen, T. F. Chen, W. P. Gong, W. Y. Xu, D. Y. Wang and Q. K. Wang, Journal of the American Ceramic Society **96** (6), 1857-1862 (2013).
55. H. L. Han, L. W. Yang, Y. X. Liu, Y. Y. Zhang and Q. B. Yang, Optical Materials **31** (2), 338-341 (2008).

56. L. Jiang, S. Xiao, X. Yang, J. Ding and K. Dong, Applied Physics B-Lasers and Optics **107** (2), 477-481 (2012).
57. L. Liu, Y. X. Wang, X. R. Zhang, K. Yang, Y. F. Bai, C. H. Huang, W. L. Han, C. L. Li and Y. L. Song, Optical Materials **33** (8), 1234-1238 (2011).
58. L. Liu, Y. X. Wang, X. R. Zhang, K. Yang, Y. F. Bai, C. H. Huang and Y. L. Song, Optics Communications **284** (7), 1876-1879 (2011).
59. J. H. Chung, J. H. Ryu, J. W. Eun, J. H. Lee, S. Y. Lee, T. H. Heo and K. B. Shim, Materials Chemistry and Physics **134** (2-3), 695-699 (2012).
60. D. H. Kim, J. H. Ryu, J. H. Chung, K. B. Shim and S. Y. Cho, Journal of the Electrochemical Society **158** (11), J345-J348 (2011).
61. J. H. Chung, J. I. Lee, S. L. Ryu and J. H. Ryu, Ceramics International **39**, S369-S372 (2013).
62. J. H. Kim, H. Choi, E. O. Kim, H. M. Noh, B. K. Moon and J. H. Jeong, Optical Materials **38**, 113-118 (2014).
63. T. V. Gavrilovic, D. J. Jovanovic, L. V. Trandafilovic and M. D. Dramicanin, Optical Materials **45**, 76-81 (2015).
64. T. V. Gavrilovic, D. J. Jovanovic, V. M. Lojpur, V. Dordevic and M. D. Dramicanin, Journal of Solid State Chemistry **217**, 92-98 (2014).
65. V. Mahalingam, R. Naccache, F. Vetrone and J. A. Capobianco, Optics Express **20** (1), 111-119 (2012).
66. L. Mukhopadhyay, V. K. Rai, R. Bokolia and K. Sreenivas, Journal of Luminescence **187**, 368-377 (2017).
67. M. Mondal, V. K. Rai, C. Srivastava, S. Sarkar and R. Akash, Journal of Applied Physics **120** (23) (2016).
68. X. X. Luo and W. H. Cao, Journal of Materials Research **23** (8), 2078-2083 (2008).
69. W. Y. He, X. F. Wang, J. Zheng and X. H. Yan, Materials Research Innovations **18** (5), 376-379 (2014).
70. A. K. Singh, S. K. Singh and S. B. Rai, Rsc Advances **4** (51), 27039-27061 (2014).
71. F. Auzel, Chemical Reviews **104** (1), 139-173 (2004).
72. F. Wang, J. A. Wang and X. G. Liu, Angewandte Chemie-International Edition **49** (41), 7456-7460 (2010).
73. R. D. Shannon, Acta Crystallographica Section A **32** (SEP1), 751-767 (1976).
74. M. A. Pena and J. L. G. Fierro, Chemical Reviews **101** (7), 1981-2017 (2001).
75. Y. Gao and Z. Y. Tang, Small **7** (15), 2133-2146 (2011).
76. H. Dong, L. D. Sun and C. H. Yan, Chemical Society Reviews **44** (6), 1608-1634 (2015).
77. M. Haase and H. Schafer, Angewandte Chemie-International Edition **50** (26), 5808-5829 (2011).
78. F. Vetrone, J. C. Boyer, J. A. Capobianco, A. Speghini and M. Bettinelli, Chemistry of Materials **15** (14), 2737-2743 (2003).
79. H. Guo, N. Dong, M. Yin, W. P. Zhang, L. R. Lou and S. D. Xia, Journal of Physical Chemistry B **108** (50), 19205-19209 (2004).
80. S. L. Gai, P. P. Yang, D. Wang, C. X. Li, N. Niu, F. He and X. B. Li, Crystengcomm **13** (17), 5480-5487 (2011).
81. I. N. Stanton, J. A. Ayres and M. J. Therien, Dalton Transactions **41** (38), 11576-11578 (2012).
82. T. Fan, Q. Y. Zhang and Z. H. Jiang, Journal of Optics **13** (1) (2011).
83. G. Y. Chen, Y. Liu, Z. G. Zhang, B. Aghahadi, G. Somesfalean, Q. Sun and F. P. Wang, Chemical Physics Letters **448** (1-3), 127-131 (2007).
84. G. Y. Chen, Y. G. Zhang, G. Somesfalean, Z. G. Zhang, Q. Sun and F. P. Wang, Applied Physics Letters **89** (16) (2006).
85. J. H. Chung, S. Y. Lee, K. B. Shim, S. Y. Kweon, S. C. Ur and J. H. Ryu, Applied Physics a-Materials Science & Processing **108** (2), 369-373 (2012).

86. L. N. Guo, Y. H. Wang, Z. H. Zou, B. Wang, X. X. Guo, L. L. Han and W. Zeng, Journal of Materials Chemistry C **2** (15), 2765-2772 (2014).
87. Y. B. Wang, T. Wei, X. W. Cheng, H. Ma, Y. Pan, J. Xie, H. Q. Su, X. J. Xie, L. Huang and W. Huang, Journal of Materials Chemistry C **5** (14), 6 (2017).
88. L. N. Guo, Y. H. Wang, Y. Z. Wang, J. Zhang, P. Y. Dong and W. Zeng, Nanoscale **5** (6), 2491-2504 (2013).
89. Q. Cheng, J. H. Sui and W. Cai, Nanoscale **4** (3), 779-784 (2012).
90. H. Lin, D. K. Xu, D. D. Teng, S. H. Yang and Y. L. Zhang, New Journal of Chemistry **39** (4), 2565-2572 (2015).
91. M. Hu, D. D. Ma, Y. Z. Cheng, C. C. Liu, Z. P. Zhang, Y. J. Cai, S. Wu and R. F. Wang, Journal of Materials Chemistry B **5** (14), 2662-2670 (2017).
92. G. Will, *Powder Diffraction: The Rietveld Method and the Two Stage Method to Determine and Refine Crystal Structures from Powder Diffraction Data*. (Springer Berlin Heidelberg, 2010).
93. D. B. Williams and C. B. Carter, *Transmission Electron Microscopy: A Textbook for Materials Science*. (Springer US, 2009).
94. L. Reimer, *Transmission Electron Microscopy: Physics of Image Formation and Microanalysis*. (Springer Berlin Heidelberg, 2014).
95. R. Levinson and R. S. o. Chemistry, *More Modern Chemical Techniques*. (Royal Society of Chemistry, 2001).
96. B. C. Smith, *Fundamentals of Fourier Transform Infrared Spectroscopy, Second Edition*. (CRC Press, 2011).
97. A. W. Coats and J. P. Redfern, Analyst **88** (105), 906-& (1963).
98. S. Hofmann, *Auger- and X-Ray Photoelectron Spectroscopy in Materials Science: A User-Oriented Guide*. (Springer Berlin Heidelberg, 2012).
99. G. Blasse and B. C. Grabmaier, *Luminescent materials*. (Springer-Verlag, 1994).
100. H. X. Mai, Y. W. Zhang, L. D. Sun and C. H. Yan, Journal of Physical Chemistry C **111** (37), 13721-13729 (2007).
101. F. Vetrone, J. C. Boyer, J. A. Capobianco, A. Speghini and M. Bettinelli, Journal of Applied Physics **96** (1), 661-667 (2004).
102. T. Danger, J. Koetke, R. Brede, E. Heumann, G. Huber and B. H. T. Chai, Journal of Applied Physics **76** (3), 1413-1422 (1994).
103. S. Balabhadra, M. L. Debasu, C. D. S. Brites, R. A. S. Ferreira and L. D. Carlos, Journal of Luminescence **189**, 64-70 (2017).
104. D. K. Chatteriee, A. J. Rufalhah and Y. Zhang, Biomaterials **29** (7), 937-943 (2008).
105. J. C. Boyer and F. van Veggel, Nanoscale **2** (8), 1417-1419 (2010).
106. O. A. Savchuk, J. J. Carvajal, J. Massons, M. Aguilo and F. Diaz, Carbon **103**, 134-141 (2016).
107. C. Wurth and U. Resch-Genger, Applied Spectroscopy **69** (6), 749-759 (2015).
108. Z. S. Chen, W. P. Gong, T. F. Chen and S. L. Li, Bulletin of Materials Science **34** (3), 429-434 (2011).
109. J. H. Wu, Y. J. Song, B. N. Han, J. Wei, Z. R. Wei and Y. M. Yang, Rsc Advances **5** (61), 49356-49362 (2015).
110. L. N. Guo, X. Zheng, S. Zhang, B. L. Zhao and Y. H. Wang, Materials Research Bulletin **86**, 1-4 (2017).
111. L. D. Sun, C. Qian, C. S. Liao, X. L. Wang and C. H. Yan, Solid State Communications **119** (6), 393-396 (2001).
112. J. Chen, C. H. Li, Z. Hui and Y. G. Liu, Inorganic Chemistry **56** (3), 1144-1151 (2017).
113. M. Y. Peng, X. W. Yin, P. A. Tanner, C. Q. Liang, P. F. Li, Q. Y. Zhang and J. R. Qiu, Journal of the American Ceramic Society **96** (9), 2870-2876 (2013).
114. C. C. Lin and R. S. Liu, Journal of Physical Chemistry Letters **2** (11), 1268-1277 (2011).

115. T. Andelman, S. Gordonov, G. Busto, P. V. Moghe and R. E. Riman, Nanoscale Research Letters **5** (2), 263-273 (2010).
116. A. P. Dementjev, A. de Graaf, M. C. M. van de Sanden, K. I. Maslakov, A. V. Naumkin and A. A. Serov, Diamond and Related Materials **9** (11), 1904-1907 (2000).
117. T. L. Barr and S. Seal, Journal of Vacuum Science & Technology a-Vacuum Surfaces and Films **13** (3), 1239-1246 (1995).
118. K. J. Boyd, D. Marton, S. S. Todorov, A. H. Albayati, J. Kulik, R. A. Zuhr and J. W. Rabalais, Journal of Vacuum Science & Technology a-Vacuum Surfaces and Films **13** (4), 2110-2122 (1995).
119. S. Bhattacharyya, J. Hong and G. Turban, Journal of Applied Physics **83** (7), 3917-3919 (1998).
120. D. Majumdar and D. Chatterjee, Journal of Applied Physics **70** (2), 988-992 (1991).
121. R. P. Vasquez, M. C. Foote and B. D. Hunt, Journal of Applied Physics **66** (10), 4866-4877 (1989).
122. R. H. Page, K. I. Schaffers, P. A. Waide, J. B. Tassano, S. A. Payne, W. F. Krupke and W. K. Bischel, Journal of the Optical Society of America B-Optical Physics **15** (3), 996-1008 (1998).
123. D. O. Faulkner, S. Petrov, D. D. Perovic, N. P. Kherani and G. A. Ozin, Journal of Materials Chemistry **22** (46), 24330-24334 (2012).
124. Y. M. Yang, C. Mi, F. Y. Jiao, X. Y. Su, X. D. Li, L. L. Liu, J. Zhang, F. Yu, Y. Z. Liu and Y. H. Mai, Journal of the American Ceramic Society **97** (6), 1769-1775 (2014).
125. M. Kaiser, C. Wurth, M. Kraft, I. Hyppanen, T. Soukka and U. Resch-Genger, Nanoscale (2017).
126. G. Y. Chen, H. L. Qju, P. N. Prasad and X. Y. Chen, Chemical Reviews **114** (10), 5161-5214 (2014).
127. M. Pollnau, D. R. Gamelin, S. R. Luthi, H. U. Gudel and M. P. Hehlen, Physical Review B **61** (5), 3337-3346 (2000).
128. J. F. Suyver, A. Aebischer, S. Garcia-Revilla, P. Gerner and H. U. Gudel, Physical Review B **71** (12) (2005).
129. L. Marciniak, K. Waszniewska, A. Bednarkiewicz, D. Hreniak and W. Strek, Journal of Physical Chemistry C **120** (16), 8877-8882 (2016).
130. W. Zheng, P. Huang, D. T. Tu, E. Ma, H. M. Zhu and X. Y. Chen, Chemical Society Reviews **44** (6), 1379-1415 (2015).
131. A. M. Pires, S. Heer, H. U. Gudel and O. A. Serra, Journal of Fluorescence **16** (3), 461-468 (2006).
132. V. Singh, V. K. Rai, K. Al-Shamery, M. Haase and S. H. Kim, Applied Physics a-Materials Science & Processing **113** (3), 747-753 (2013).